UNIVERSITY OF OKLAHOMA

GRADUATE COLLEGE

GEOMECHANICAL RESERVOIR CHARACTERIAZATION AND APPLICATIONS

A THESIS

SUBMITTED TO THE GRADUATE FACULTY

in partial fulfillment of the requirements for the

Degree of

MASTER OF SCIENCE

By

JIMAN LIU
Norman, Oklahoma
2017

GEOMECHANICAL RESERVOIR CHARACTERIAZATION AND APPLICATIONS

A THESIS APPROVED FOR THE
MEWBOURNE SCHOOL OF PETROLEUM AND GEOLOGICAL ENGINEERING

BY

_____
Dr. Ahmad Ghassemi, Chair

_____
Dr. Catalin Teodoriu

_____
Dr. Xingru Wu

Dedication

This thesis is dedicated to my mom, my baby Eric and my husband Luchao Jin.

Thank you for the pleasant surprise and endless love.

Acknowledgements

First of all, I want to express my gratitude to my advisor Dr. Ahmad Ghassemi for steering me into the area of Rock Mechanics. His patience and generous guidance always inspire me to continue when I feel frustrated. The attitudes of Dr. Ghassemi in research and life have become a model for my academic and personal life, leading me to pursue higher achievements. I would also thank Dr. Catalin Teodoriu and Dr. Xingru Wu and I am gratefully indebted to their valuable comments on this thesis. I am thankful to my colleagues in the group. It was joyful to work with them together.

Moreover, I would like to thank the faculty and staff members of the Mewbourne School of Petroleum and Geological Engineering for their dedication to providing the outstanding education and their support.

Finally, thanks to my husband Luchao for his endless love and my baby who is a gift to us.

Table of Contents

List of Tables

List of Figures

Abstract

The Mechanical Earth Model (MEM) is gaining attention in the oil and gas industry recently since utilizing horizontal well and multistage fracturing technologies requires understanding of the reservoir geomechanical properties. This thesis constructs a 3D Mechanical Earth Model (MEM) for a basin in Oklahoma. 1D MEMs that describe the rock properties, pore pressure and stress states for each well are first constructed. A 3D MEM is then generated incorporating the geological conditions through stratigraphy modeling, structural framework construction, property modeling as well as fracture modeling. A 3D sector model is then cut out to perform case studies. Wellbore breakout analysis is conducted by coupling the sector MEM with a finite element model to identify the breakouts and drilling-induced cracks and their positions. The results are analyzed and are calibrated by comparing the borehole image logs and the in-situ stresses as inputs from the 3D MEM so that the 3D MEM can be used for further calculations. Another case study is to model the hydraulic fracturing by incorporating the sector MEM into StimPlan, a hydraulic fracturing modeling software. The impacts of injection rate and volume on fracture shapes are studied.

Chapter 1 Introduction

Earth modeling is a technique integrating geophysical, geological and reservoir engineering knowledge. Conventional earth models characterize reservoir with geophysical, structural, sedimentary and reservoir data, which is of high probability for being representative of the reservoir (Samson et al., 1998). Because of these attributes, oil and gas industry is heavily relying on earth modeling in reservoir exploration as well as development.

In recent years, advances in multiple stage fracturing and horizontal well drilling technologies lead to the commercialized development of unconventional reservoirs. Unlike the development of the conventional reservoir, geomechanical properties in the target unconventional reservoir play a critical role in fracturing stimulation design as well as horizontal well drilling. Because of these demands, the Mechanical Earth Model (also known as MEM) is gaining attentions in the oil and gas industry. Plumb et al., (2000) defined the MEM as a numerical representation of the state of stress and rock mechanical properties for a specific stratigraphic section in a field or basin. The MEM not only includes reservoir properties such as rock type, fluid saturations, porosity and permeability et al., but also combines geomechanical properties such as in situ stress states, Poisson's Ratio and Young's Modulus, et al.

There are two crucial components in the drilling process, which are minimizing non-productive time and minimizing the risk of pore pressure or wellbore stability related problems, requiring an understanding of the geomechanics of a target reservoir. Plumb et al., (2000) summarized the relationship between drilling decisions and the mechanical earth model as in Table 1-1, from which it can be found that the MEM has a

great value in drilling planning and execution decisions. There are also many other studies which have applied the MEM to reduce well costs, minimize drilling risks, and conduct wellbore stability in various fields (Lee et al., 2003 and 2009; Afsari et al., 2009 and 2010; Perchikolaee et al., 2010). Fattahpour et al. (2012) built a mechanical earth model and applied it to well design and construction for field development by the generation of a drilling mud weight strategy based on the MEM. Doyen et al. (2003) developed a methodology to propagate uncertainties in seismic pore pressure prediction using a 3D Probabilistic Mechanical Earth Model (P-MEM), which is useful in helping accurately estimate pore pressure for safe well planning. MEM is also beneficial to provide information for hydraulic fracturing simulation. Properties such as minimum horizontal stress, closure stress and rock mechanical properties like Young's modulus, Poisson's ratio and brittleness, which can be computed from MEM, are necessary for hydraulic fracturing modeling (Liang et al., 2016). Coupling MEM and discrete fracture network (DFN) is also able to provide more representative reservoir characterization for hydraulic fracturing modeling and design (Spence et al., 2014).

In this thesis, 1D MEMs that describe the rock properties, pore pressure, and stress states for each individual well are first constructed and a 3D MEM is then generated incorporating the geological conditions. The interesting formation is a section of limestone located in central Oklahoma. Relevant theories and methodologies for data processing and model construction are described in Chapter 2. The constructed 1D and 3D mechanical earth models are presented in Chapter 3. Chapter 4 shows two application cases using the MEMs for calculating breakout and drilling-induced cracks

analysis along the wellbore with a finite element method program and hydraulic fracturing modeling using StimPlan software.

Table 1-1 Relationship between drilling decisions and the mechanical earth model (after Plumb et al., 2000)

Drilling Decision	Earth Stresses, Pore Pressure	Rock Failure Mechanisms	Rock Mechanical Parameters	Geological Structure Stratigraphy
Well location	X	X	X	X
Rig selection and BOP rating	X			
Trajectory analysis	X	X	X	X
Casing design	X			X
Safe mud weight	X			
Wellbore stability	X	X	X	X
Drilling fluids	X	X	X	X
Drilling practices	X	X	X	X
Cementing strategy	X			
Bit selection			X	X

Chapter 2 Theories and Methodologies

2.1 Types of Data

One of the most important features of the mechanical earth model is that it integrates earth sciences with geomechanics or rock mechanics data and theories. Therefore, to construct a MEM, comprehensive data sources are required, including the geological information of the field or basin, data from drilling, well logging, production, stimulation, as well as data from core tests in the lab and so on. They are widely used in 1D, 2D and 3D modeling software for the construction of mechanical earth models. The geological information of the field or basin helps to visualize the features of the reservoir and to control the data anisotropy in different directions.

2.2 Applied methods

2.2.1 Stress around the wellbore

The Kirsch (1898) solution offers a mathematical expression for the effective tangential stress around a wellbore in terms of σ_{hmin} and σ_{Hmax}, given as Eq. 2-1:

$$\sigma_{\theta\theta} = \sigma_{h\min}[(1+\frac{\sigma_{H\max}}{\sigma_{h\min}})+(1-\frac{\sigma_{H\max}}{\sigma_{h\min}})2\cos(2\theta)]-\alpha P_p - P_w \tag{2-1}$$

where $\boldsymbol{\theta}$ is the angle measured counter clockwise from the greatest principal stress in a wellbore cross section; $\boldsymbol{P_w}$ is the wellbore pressure assumed to be the same as the pore pressure $\boldsymbol{P_p}$ so that the effective radial stress at the wellbore wall is zero; $\boldsymbol{\alpha}$ is the Biot coefficient for failure analysis which is taken to be 1. The overburden is assumed to be a principal stress whose axis is the wellbore and the tangential stress can be compressive or tensile. For the case of compressive tangential stress the rock will fail in shear if $\boldsymbol{\sigma_{\theta\theta}}$ is larger than the uniaxial compressive strength; while for the tensile

tangential stress, the rock at the wellbore will fail in tension if the tensile strength is exceeded. The uniaxial compressive strength $\boldsymbol{UCS}$ and the tensile strength $\boldsymbol{T}$ is determined experimentally in the laboratory or derived from well log correlations.

The possibility of breakouts occurring may be solved with different methods for depending on the available data by replacing $\boldsymbol{\sigma_{\theta\theta}}$ with the appropriate rock strength or allowing $\boldsymbol{\theta}$ to be $\mathbf{90}°$, which is the azimuth of the minimum principal stress. With the available fracture test data, the stresses can then be solved for using the ratio. Under the condition that no breakouts or tensile fractures are visible in borehole image logs and no fracture tests constrain the least horizontal stress, Eq. 2-1 can be used with the tensile and compressive rock strengths (determined in the lab or values taken from similar rock samples) as input to generate a system of equations which can then be used to constrain the horizontal stresses (Brady and Brown, 1985; Moos and Barton, 1990):

$$\sigma_{\theta\theta\max} = 3\sigma_{H\max} - \sigma_{h\min} - \alpha P_p - P_w \geq UCS \tag{2-2}$$

$$\sigma_{\theta\theta\min} = 3\sigma_{h\min} - \sigma_{H\max} - \alpha P_p - P_w \leq -T \tag{2-3}$$

The overburden is taken to be a principal stress whose axis is vertical. For a vertical wellbore then, the principal horizontal stresses lay in the plane of a cross section. If drilling induced breakouts or tensile fractures are visible in image logs, these can be used to characterize the stress directions. Based on the Kirsch solution, a drilling-induced tensile fracture appears at the azimuth of the maximum horizontal stress while breakouts appear at the azimuth of the least horizontal stress. Other methods using well logs are available such as using the crossed dipole sonic log to determine stress orientations. If no means to calculate the stress directions at the wellbore are available, then regional stress directions can be used.

2.2.2 Anisotropy for laminated formation

In this study, the laminated formations such as C shale with anisotropic features are studied as well. They are considered as transversely isotropic (TI). The sonic logs of the wells are used to calculate stiffness matrix of the rocks and to further calculate the rock properties. Five independent parameters are needed to describe the stiffness matrix of transversely isotropic material. However, the five independent parameters cannot all be measured in this case due to the limitation of the logging tools. So the stiffness matrixes are calculated based on the data from the vertical wells, and the missing information is estimated from the data of the nearby horizontal wells.

The velocities of the wave propagations in a TI medium are given as

$$
\begin{aligned}
V_p(\theta) &= (2\rho)^{-\frac{1}{2}}\sqrt{C_{11}\sin^2\theta + C_{33}\cos^2\theta + C_{44} + K(\theta)} \\
V_{SV}(\theta) &= (2\rho)^{-\frac{1}{2}}\sqrt{C_{11}\sin^2\theta + C_{33}\cos^2\theta + C_{44} - K(\theta)} \\
V_{SH}(\theta) &= \rho^{-\frac{1}{2}}\sqrt{C_{66}\sin^2\theta + C_{44}\cos^2\theta} \\
K(\theta) &= \sqrt{[(C_{11}-C_{44})\sin^2\theta - (C_{33}-C_{44})\cos^2\theta]^2 + (C_{13}+C_{44})^2\sin^2 2\theta}
\end{aligned}
\qquad \text{(2-4)}
$$

where θ is the angle between the directions of the primary wave and the normal of the isotropic plane of the medium. The stiffness coefficients are a function of the stoneley tube velocity (Norris and Sinha, 1993).

$$
\rho_f \frac{V_T^2(\theta)V_f^2}{V_f^2 - V_T^2(\theta)} = \frac{1}{8}(C_{11}\sin^4\theta - 2C_{13}\sin^4(\theta) + C_{33}\sin^4\theta) + C_{44}(1-\cos^2\theta - \frac{\sin^4\theta}{2}) + C_{66}\cos^2\theta \qquad \text{(2-5)}
$$

where V_T is the stoneley wave velocity, V_f is the drilling fluid velocity, and ρ_f is the drilling fluid density.

Propagation of the primary wave and fast and slow shear waves are schematically described in Figure 2-1.

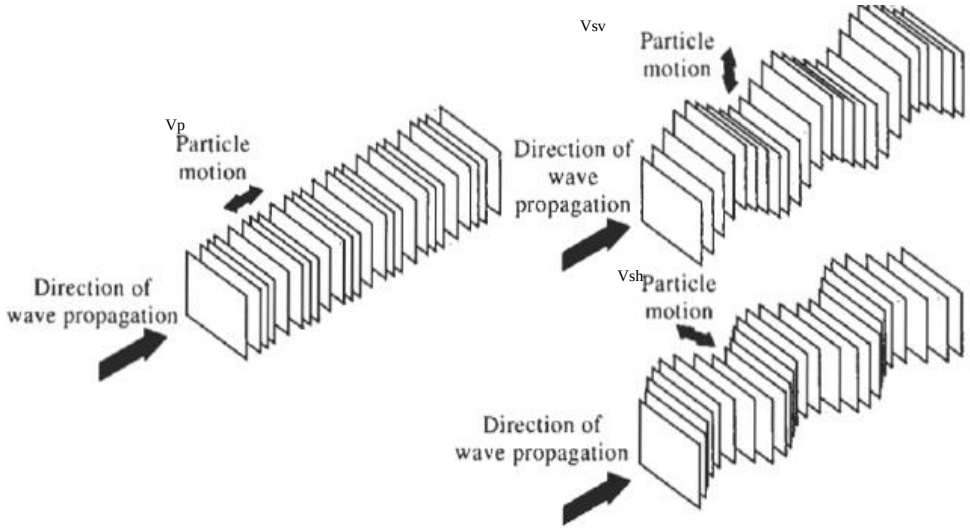

Figure 2-1 Primary and shear wave modes (after Hudson and Harrison, 1997)

2.3 Workflow

Fig. 2-2 summarizes a general workflow to construct a 3D mechanical earth model. As mentioned in previous sections, mechanical earth models integrated data from multiple resources, so the first step is to gather data. Then the relevant data is imported into the software to set up the model. In this thesis, the Schlumberger Petrel software is used. One necessary step is to calibrate the depth of data from various resources such as well logs and core characterization. Then the overburden stress and pore pressure, mechanical rock properties, in-situ stress, as well as failure mechanisms are calculated and input into the software. With this information, 1D mechanical earth models for wells can be constructed.

With the constructed 1D mechanical earth models of various wells, a 3D mechanical earth model can be built with modeling the geological properties, which may come from a seismic survey or geology reservoir characterization. The next step is to conduct structure modeling as well as property modeling, after which a 3D mechanical earth

model is constructed. More detailed modeling procedures following the workflow as Fig. 2-2 will be described in Chapter 3.

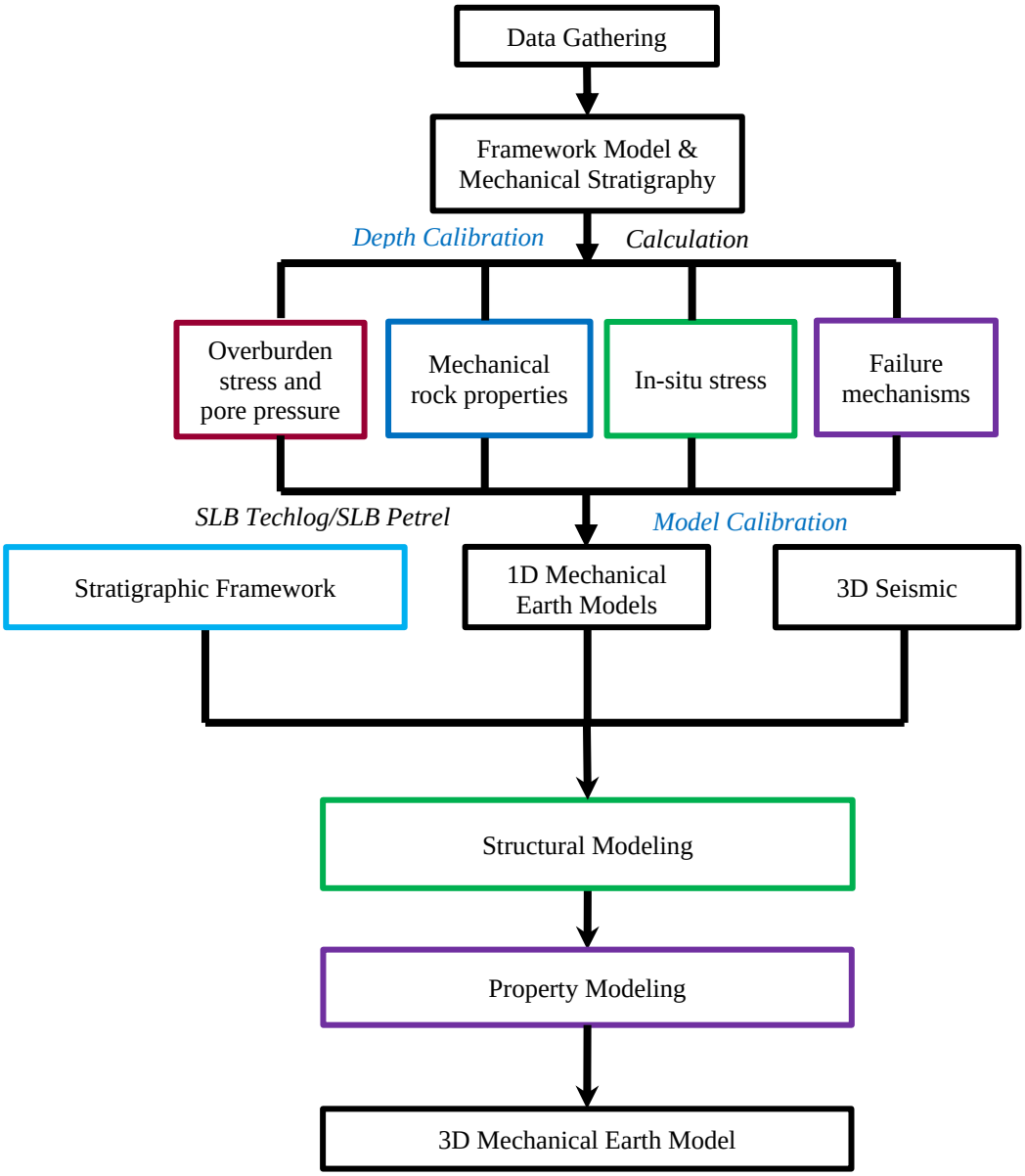

Figure 2-2 3D mechanical earth model workflow (Janis, 2016)

Chapter 3 Construction of Mechanical Earth Model

Following the theories and methodologies, as described in Chapter 2, a 3D mechanical earth model is constructed for central Oklahoma. The target formations are limestone and shale, but the formations above the target limestone and below the target shale are also modeled in this project to offer necessary parameters of confining zones and boundary condition for further simulation applications. 1D MEMs that describe the rock properties, pore pressure, and stress status for each individual well were firstly constructed and a 3D MEM was then generated incorporating the geological conditions.

3.1 Data audit and model set up

In order to construct the model, the required data is first audited to confirm all the necessary information are included in the database. Table 3-1 summarizes the available data. In this work, 19 wells in total are studied including 13 vertical wells and 6 horizontal wells. The log data to construct the mechanical earth model is available for 9 wells; borehole image logs are available for 3 wells and hydraulic fracturing reports are available for two of the horizontal wells. Extra work, references, and assumptions are necessary when important information is lacked and cannot be measured with current logging tools.

This 3D mechanical earth model (3D MEM) is constructed in Schlumberger Petrel 2014 software. Field units are used in this model set up. A coordinate reference system (CRS) for this model is selected, based on the well locations defined during geology measurement. Relevant data is then imported into the Petrel software.

Table 3-1 Data audit summary

Well Name	Type	Log data for MEM	Core Gamma Ray	Borehole Image Log	Hydraulic fracturing reports	Microseismic data
Well 1	Horizontal					
Well 2	Vertical	X	X	X		
Well 3	Vertical					
Well 4	Vertical	X				
Well 5	Vertical	X				
Well 6	Vertical	X	X			
Well 7	Vertical	X		X		
Well 8	Vertical					
Well 9	Vertical	X				
Well 10	Vertical					
Well 11	Vertical					
Well 12	Horizontal				X	X
Well 13	Horizontal	X		X	X	X
Well 14	Vertical					
Well 15	Horizontal					X
Well 16	Vertical	X	X			
Well 17	Horizontal				X	
Well 18	Horizontal				X	
Well 19	Vertical	X	X			

3.2 Mechanical stratigraphy

In this step, the well depths of the log data are calibrated with the cores. Then the formation types are identified for each well.

3.2.1 Well depth calibration

The depth of well log data often gets errors when the log data is measured during drilling and logging operation in the field. It is necessary to calibrate the log depth before to the logs being used for further calculation, to prevent depth error caused by line stretching during wireline oepration. The depth of Gamma ray is often chosen to do the well depth calibration, since it is mostly measured in well logging and its value of core samples can be easily measured by using surface tools. As shown in Fig. 3-1, the

left figure shows the gamma ray from well logs, and the right figure shows the gamma ray from cores. The depth of Gamma ray logs is adjusted to ensure the Gamma ray value at a certain depth is the same as that from the core data. In this way the depth of logs is calibrated. There are four sets of Gamma ray from core data available in this project as shown in Table 3-1. All these four well logs are calibrated and the depth deviations are listed in the Table 3-2.

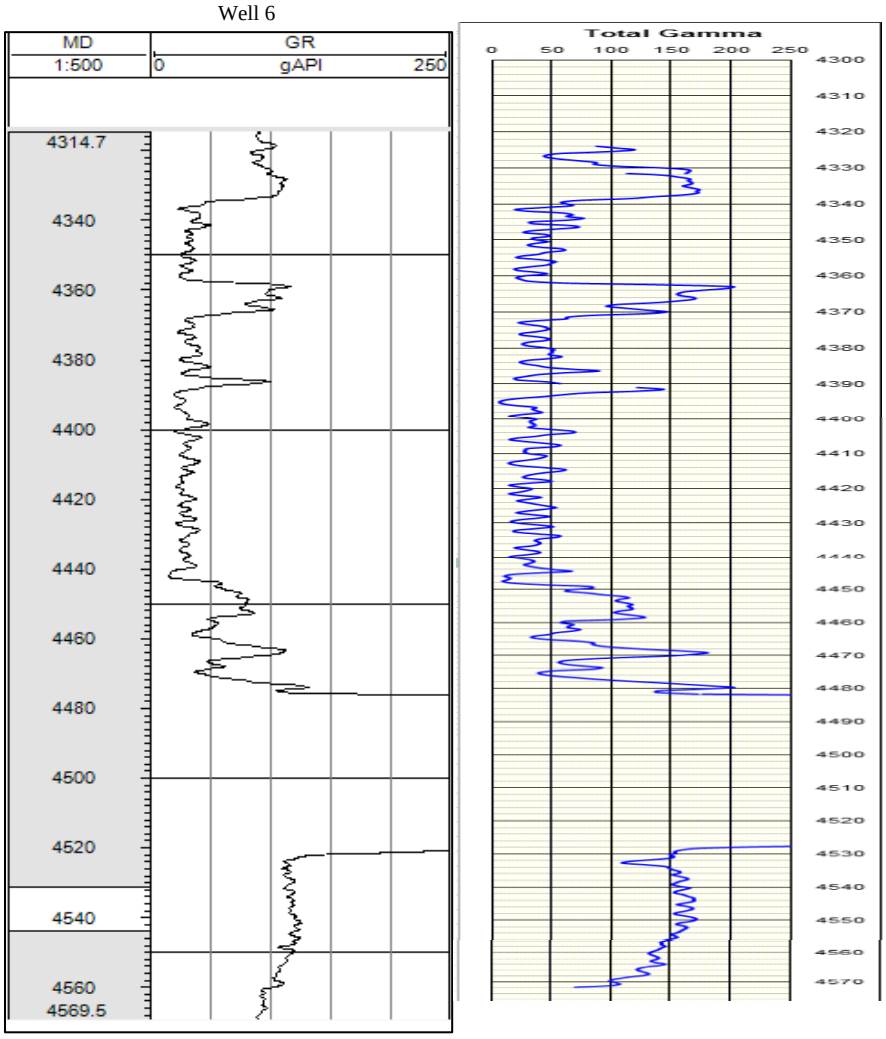

Figure 3-1 Depth calibration of Well 6

(Left: Log Gamma Ray Right: Core Gamma Ray)

Table3-2 Well depth deviation

Well Name	Depth Deviation, ft
Well 2	2.97
Well 6	-5.50
Well 16	-1.28
Well 19	-9.45

3.2.2 Well cross sections and well top correlation

Fig. 3-2 shows the reservoir polygon and the cross section in a 2D view. The cross section presents the wells in the reservoir from west to east. The gamma ray, porosity, density and rock property logs of each wells are studied to identify formation zones with similar properties as shown in the left hand of Figure 3-3. Then the top depth of the formations in each well are connected, which is called well top correlation. The core descriptions from the geologists are also referred for validation in well top correlation, as shown in the right hand of Figure 3-3.

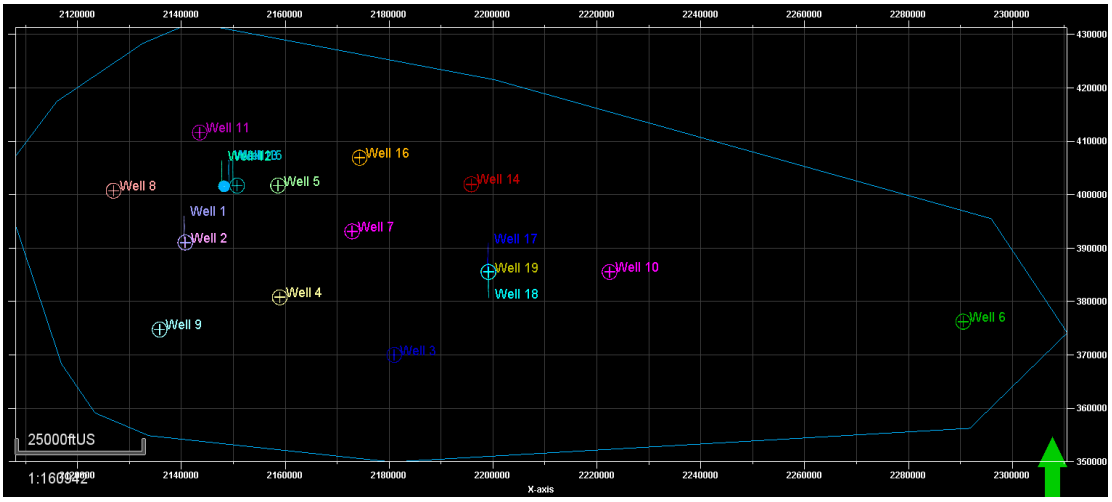

Figure 3-2 2D view of the cross section of the reservoir

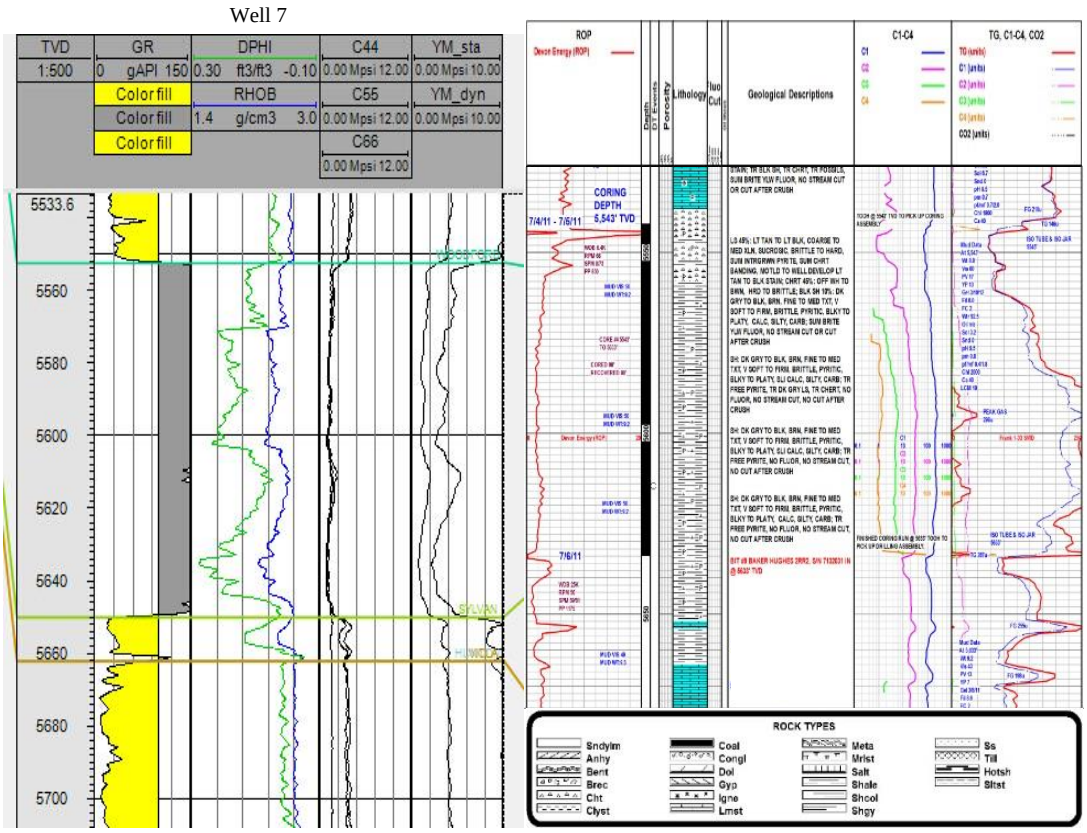

Figure 3-3 Well logs of rock properties vs. geological core description

After that, the formation types along the wells are identified (Figure 3-4). In this basin, there are four formation zones: above top B is A limestone layer; between top B and C is B limestone, which is the target formation to be studied in this work; between top C and F are two different shale layers; below top F is another limestone. Then associated calculation methods for the rock properties are applied to construct the 1D MEMs.

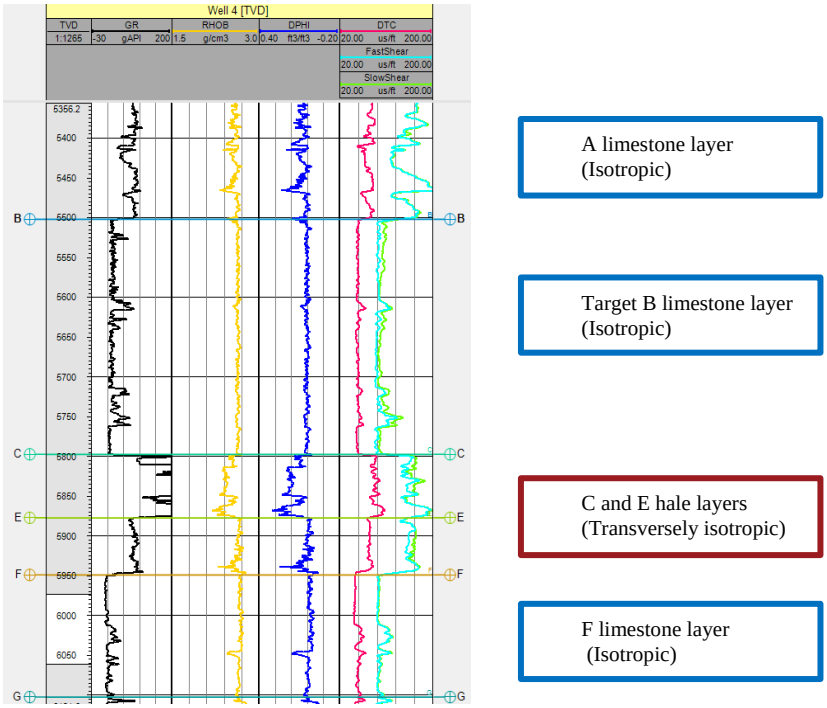

Figure 3-4 Formation types of a well

3.3 Construction of 1D Mechanical Earth Model

Constructing 1D mechanical earth models for wells is a necessary step prior to build the 3D model. 1D mechanical earth models are firstly built for the 9 wells with available log data (shown in the Table 3-1), from which the overburden, pore pressure, rock properties and horizontal stresses are estimated. However, we don't have the log data from the ground surface to the reservoir depth along the wells, so the unknown parameters are assumed to be necessary in this work.

From the log data and core study and analysis, the main rock types of this study are identified as limestone and laminated shale. Therefore, relevant rock properties and calculation methods for limestone and shale were used. The limestone is considered as isotropic and the laminated shale is considered as transversely isotropic as shown in Figure 3-4.

3.3.1 Overburden

The overburden of a vertical well is calculated by integrating the formation density (RHOB), shown as Eq. 3.1. The formation density from the ground surface to the measured zones by logging tools is assumed as 1.6 g/cm^3, which is estimated by referring to the formation bulk density in the shallow depth of the zones with available data.

$$\sigma_v = \int_0^z \rho(z) g dz \tag{3-1}$$

3.3.2 Pore Pressure

Pore Pressure gradient is estimated by Eq. 3.2, after Zhang (2011), which mainly applys in rapidly subsiding basins and in rocks with low permeability:

$$P_g = OBG - \left(OBG - P_{ng}\right)\frac{(ln\emptyset_0 - ln\emptyset)}{cZ} \tag{3-2}$$

where $\emptyset$ is the porosity at depth of Z that can be obtained from sonic or density logs. $\emptyset_0$ is the porosity in the mudline. c is the compaction constant of 0.00047 from Athy (1930). P_{ng} is the hydrostatic pore pressure gradient assumed as 0.465 psi/ft. The method from Zhang (2011) predicts pore pressure basing on the depths and normal compaction trend of porosity. It presents overpressure of the formation when porosity at an interested depth is larger than the normal porosity at the same depth.

3.3.3 Rock Mechanical Properties

Since there are isotropic limestone, sandstone and transversely isotropic shale formation, calculation methods should be separately discussed.

1) Limestone formation

In the limestone formation, rock properties calculation methods for limestone are adopted according to Yasar and Erdogan (2004) and Yale and Jamieson (1994).

a) Young's Modulus:

The dynamic Young's Modulus is computed by V_p and V_s as shown in Eq. 3-3.

$$E_{dyn} = \frac{RHOB * V_s^2 (3V_p^2 - 4V_s^2)}{V_p^2 - V_s^2} \tag{3-3}$$

Yale and Jamieson (1994) measured the dynamic and static Young's modulus for limestones and dolostones. From the experimental data as shown in Fig. 3-5, it can be seen that the relationships of dynamic and static Young's modulus for limestones and dolostones are very similar (Sayers 2008). The correlation for limestones is expressed as Eq. 3-4.

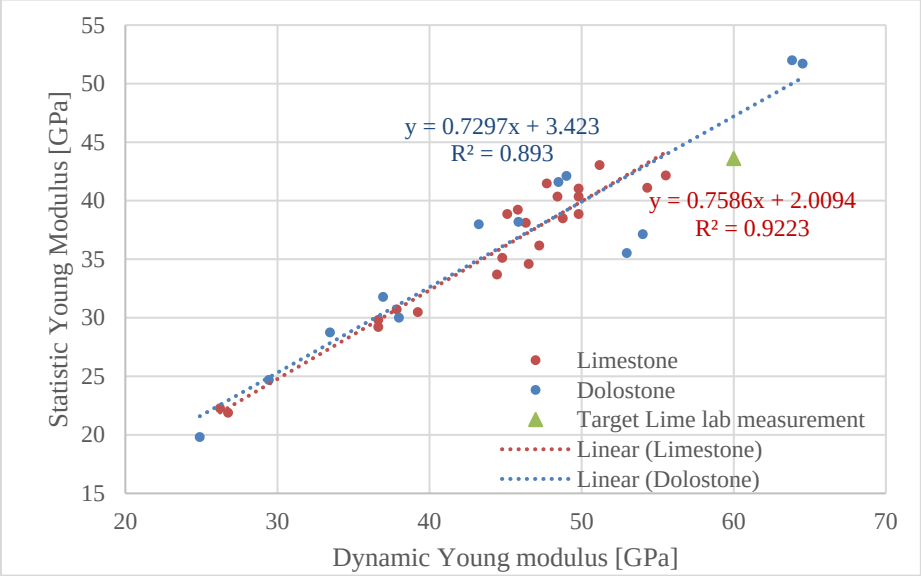

Figure 3-5 Dynamic and static Young's modulus for limestones (red) and dolostones (blue) measured by Yale and Jamieson (1994) for air-filled samples from the Hugoton and Panoma fields, Kansas

$$E_{sta} = 0.7586E_{dyn} + 2.0094 \quad (3\text{-}4)$$

b) Poisson's Ratio:

The dynamic Poisson's Ratio is calculated from V_p and V_s.

$$\nu_{dyn} = \frac{(V_p^2 - 2V_s^2)}{2(V_p^2 - V_s^2)} \quad (3\text{-}5)$$

Similar with the Young's modulus, the correlation of dynamic and static Poisson's Ratio is also studied and obtained with the experimental data measured by Yale and Jamieson (1994) (shown in Fig. 3-6). The correlation is shown as Eq. 3-6.

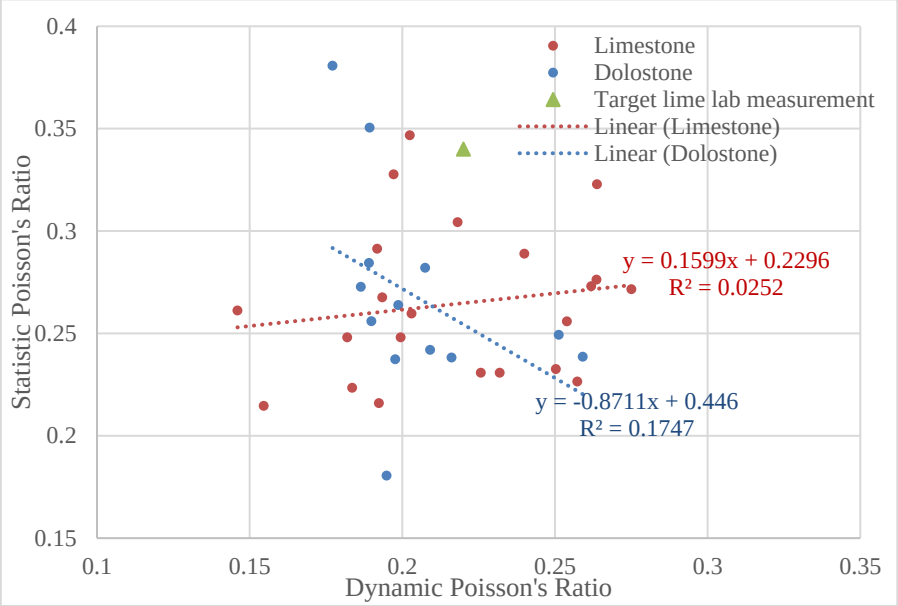

Figure 3-6 Dynamic and static Poisson's ratio for limestones (red) and dolostones (blue) measured by Yale and Jamieson (1994) for air-filled samples from the Hugoton and Panoma fields, Kansas

$$\boldsymbol{\nu}_{sta} = 0.1599\boldsymbol{\nu}_{dyn} + 0.2296 \quad (3\text{-}6)$$

c) Unconfined Compressive Strength:

Unconfined compressive strength of limestone and/or dolomite that computed from sonic wave velocity, Young's modulus and porosity is in an extraordinarily wide range with any given parameters. The correlation used in this study to calculate USC is showed in Eq. 3-7, which is a function of Young's modulus (Chang, 2006). In developing this correlation, Chang (2006) utilized a wide range of UCS data so it is more reliable.

$$USC = 13.8E_{sta}^{0.51} \tag{3-7}$$

2) Sandstone formation

a) Young's Modulus:

The dynamic Young's Modulus is calculated with the same method with limestone, as shown in Eq. 3-8. The Static Young's Modulus is computed by Eq. 3-9, following the method in Wang (2000). These correlations are suitable to calculate dynamic and static Young's modulus for hard rocks whose static Young's modulus is greater than 15 Gpa.

$$E_{dyn} = \frac{RHOB * V_s^2 (3V_p^2 - 4V_s^2)}{V_p^2 - V_s^2} \tag{3-8}$$

$$E_{sta} = 1.1530E_{dyn} - 15.1970 \tag{3-9}$$

b) Poisson's Ratio:

The dynamic Poisson's Ratio is calculated from V_p and V_s.

$$\nu_{dyn} = \frac{(V_p^2 - 2V_s^2)}{2(V_p^2 - V_s^2)} \tag{3-10}$$

and the static Poisson's Ratio is given as (Wang, 2000),

$$\nu_{sta} = 0.7\nu_{dyn} \tag{3-11}$$

c) Unconfined Compressive Strength:

Unconfined compressive strength is computed from dipole sonic data based on the Plumb empirical correlation (Bradford, et al., 1998) for sandstone reservoirs.

$$USC = 2.280 + 4.1089E_{sta} \tag{3-12}$$

3) Transversely isotropic shale formation

a) Young's Modulus and Poisson's Ratio:

There are five independent parameters to present the transverse isotropy and the stiffness matrix,

$$\begin{bmatrix} \sigma_x \\ \sigma_y \\ \sigma_z \\ \tau_{xz} \\ \tau_{yz} \\ \tau_{xy} \end{bmatrix} = \begin{bmatrix} C_{11} & C_{12} & C_{13} & & & \\ C_{21} & C_{22} & C_{23} & & & \\ C_{31} & C_{32} & C_{33} & & & \\ & & & C_{44} & & \\ & & & & C_{55} & \\ & & & & & C_{66} \end{bmatrix} \begin{bmatrix} \varepsilon_x \\ \varepsilon_y \\ \varepsilon_z \\ \gamma_{xz} \\ \gamma_{yz} \\ \gamma_{xy} \end{bmatrix}, \tag{3-13}$$

Considering the shale laminated bedding are horizontal, the vertical wells are perpendicular to the laminated beddings, while the horizontal wells are parallel to the laminated beddings. So two kinds of transversely isotropic models, as shown in Fig 3-7, are discussed in this study: vertical transversely isotropic (VTI) model and horizontal transversely isotropic (HTI) model.

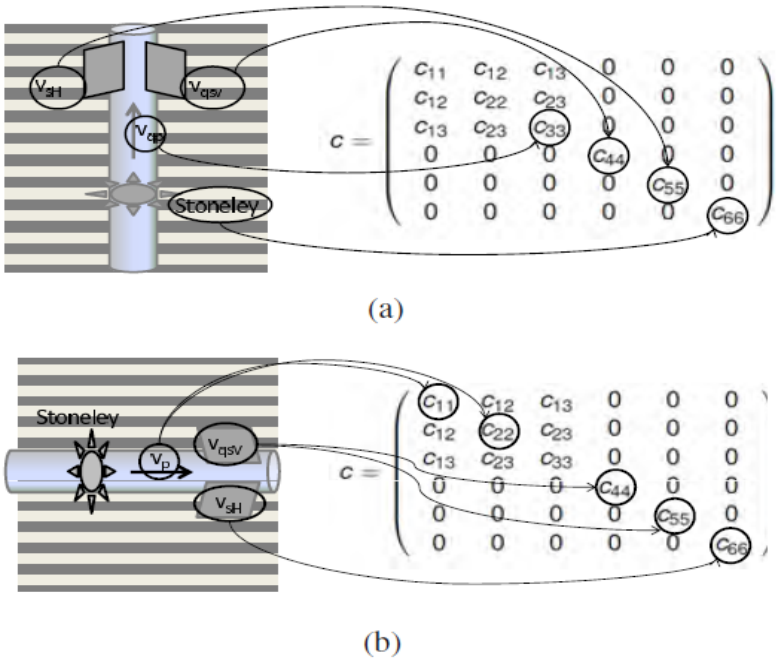

Fig 3-7 Relationship between borehole sonic velocities and stiffness tensor components of a VTI formation (a) and a HTI formation (b). (Prioul, 2012)

For a vertical well, the directions of the primary wave and the shale beds are the same, so that θ=0°.Therefore, V_p (0°) is perpendicular to shale beds, whereas the V_s fast (0°) and V_s slow (0°) are parallel to the beds. In this case, the V_s fast and V_s slow are the same, which means C_{44} equals to C_{55}. In this situation, C_{11} and C_{22} are the same but different from C_{33} in Eq. 3-13.

For this VTI medium, θ=0°

$$
\begin{aligned}
&C_{33} = \rho V_p^2(0°)\\
&C_{44} = \rho V_s^2(0°)\\
&C_{11} = C_{22} \neq C_{33}\\
&C_{44} = C_{55} \neq C_{66}\\
&2C_{66} = C_{11} - C_{12}
\end{aligned}
\qquad (3\text{-}14)
$$

For a horizontal well, the direction of the primary wave is perpendicular to the shale beds, that is θ=90°. Under this circumstance, C_{11} can be calculated from the V_p (90°)

of the horizontal well ultrasonic log. V_s slow (90°) and V_s fast (90°) are perpendicular to the fracture system and parallel to the fracture system, so that they can be used to calculate C_{44} and C_{55}. The stoneley is used to calculate C_{66}.

For HTI medium, θ=90°

$$C_{11} = C_{22} = \rho V_p^2(90°)$$
$$C_{66} = \rho V_{ss}^2(90°) \tag{3-15}$$

ANNIE approximation (Schoenberg et al., 1996) is used to simplify the matrix, which assumes that

$$C_{12} = C_{13} = C_{23} \tag{3-16}$$

The relation can be inversed and rewritten as,

$$\begin{bmatrix} \varepsilon_x \\ \varepsilon_y \\ \varepsilon_z \\ \gamma_{xz} \\ \gamma_{yz} \\ \gamma_{xy} \end{bmatrix} = \begin{bmatrix} \frac{1}{E_h} & -\frac{\nu_h}{E_h} & -\frac{\nu_v}{E_v} & & & \\ -\frac{\nu_h}{E_h} & \frac{1}{E_h} & -\frac{\nu_v}{E_v} & & & \\ -\frac{\nu_v}{E_v} & -\frac{\nu_v}{E_v} & \frac{1}{E_v} & & & \\ & & & \frac{1}{G_v} & & \\ & & & & \frac{1}{G_v} & \\ & & & & & \frac{1}{G_h} \end{bmatrix} \begin{bmatrix} \sigma_x \\ \sigma_y \\ \sigma_z \\ \tau_{xz} \\ \tau_{yz} \\ \tau_{xy} \end{bmatrix} \tag{3-17}$$

which can be solved as,

$$E_v = C_{33} - \frac{2C_{13}^2}{C_{11} + C_{12}};$$

$$E_h = \frac{(C_{11} - C_{12})(C_{11}C_{33} - 2C_{13}^2 + C_{12}C_{33})}{C_{11}C_{33} - C_{13}^2}$$

$$\nu_v = \frac{C_{13}}{C_{11} + C_{12}}$$

$$\nu_h = \frac{C_{33}C_{12} - C_{13}^2}{C_{11}C_{33} - C_{13}^2}$$

$$\frac{1}{G_v} = C_{44}$$

$$\frac{1}{G_h} = \frac{E_h}{2(1+\nu_h)} = C_{66} \qquad (3\text{-}18)$$

With the above expressions, related rock properties can be calculated.

b) Unconfined Compressive Strength

The unconfined compressive strength is computed from dipole sonic data based on the Plumb empirical correlation (Bradford, et al., 1998).

$$USC = 2.280 + 4.1089E \qquad (3\text{-}19)$$

3.3.4 In-situ stresses

The rock matrix is considered as a porous elastic material, and the minimum horizontal stress is estimated based on the poroelastic theory. In this study, the lateral strains are considered as zero, as the rock matrix is adjacent to the reservoir and under compaction. Tectonic is not considered during in-situ stress estimation, as the fault information in this area is scarce. The equation to estimate the minimum horizontal stress is shown as Eq. 3-20.

$$\sigma_h = \frac{\mathrm{E_h}}{\mathrm{E_v}} \frac{\upsilon_v}{1-\upsilon_h} (\sigma_v - \alpha P_p) + \alpha P_p + \frac{E_h}{1-\upsilon_h^2} e_{H,\min} + \frac{\upsilon_h E_h}{1-\upsilon_h^2} e_{H,\max} \qquad (3\text{-}20)$$

where σ_h is the minimum horizontal stress; E_h and E_v are the horizontal and vertical Young's modulus, respectively; υ_h and υ_v denote the horizontal and vertical Poisson's ratio; α denote the Biot's coefficient; P_p is the pore pressure; e_H is the horizontal strain.

The maximum horizontal stress is difficult to be calculated. Sayers (2009) assumed the anisotropy of the principal horizontal stresses is small, and presents the following equation to correlate the minimum and maximum horizontal stress:

$$\sigma_H = 1.03 * \sigma_h \tag{3-21}$$

The above relationship was tested by comparing the breakouts of wells against the MEM predictions in Sayers (2009). This equation may not be applicable for the studied formation, but it can be used as a first guess to calculate the maximum horizontal stress to construct the MEM. The in-situ stresses will be further calibrated by comparing the borehole image logs against the model predictions. An example will be discussed in Chapter 4. With the constructed 1D mechanical earth models of various wells, a 3D mechanical earth model can then be built with modeling the geological properties. In this work, the stratigraphy, structural framework as well as lithology and petrophysical properties are modeled.

Then the 1D MEMs are constructed. The Fig. 3-8 shows an example of the 1D MEM, the 1D MEM of well 7. The tracks from left to right are true vertical depth, gamma ray, formation density, calculated pore pressure, Young's modulus, Poisson's ratio, uniaxial compressive strength and in-situ stress respectively.

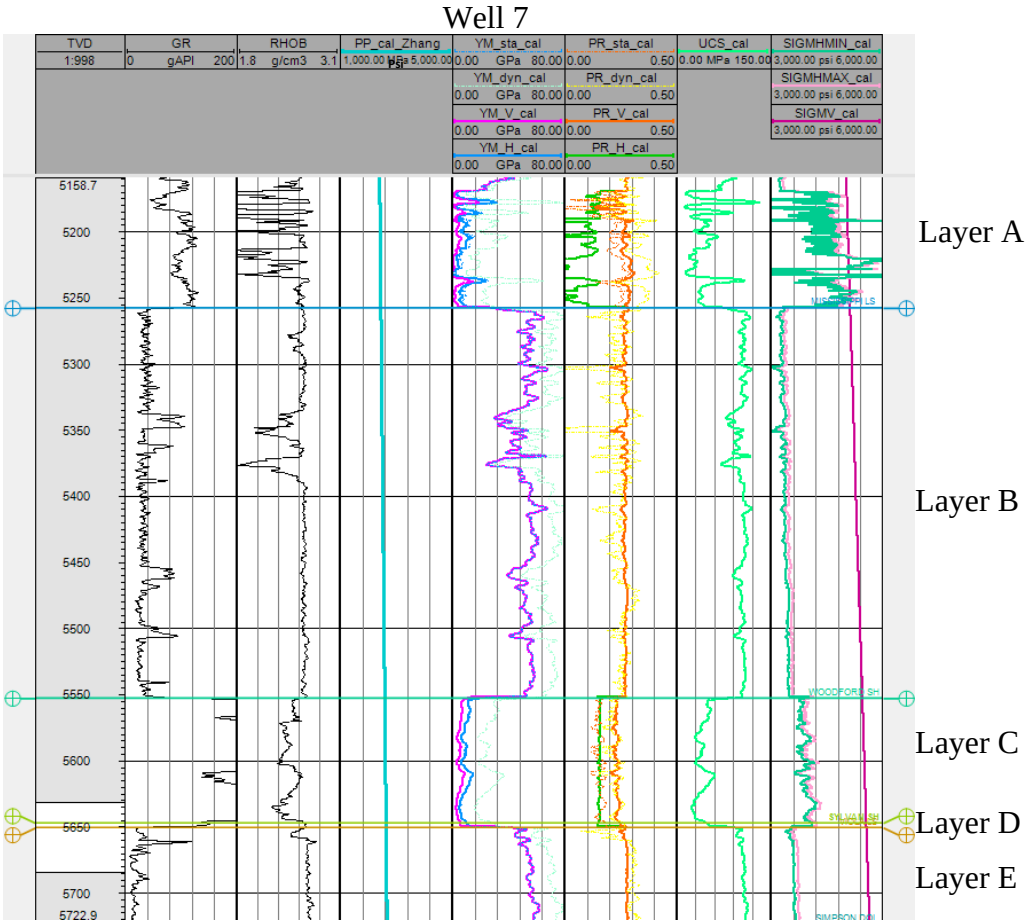

Figure 3-8 1D MEM of Well 7

3.4 Stratigraphy Modeling

As described in Chapter 1, the target formation is located in central Oklahoma. According to Dolton and Finn (1989), the reservoir is located on the south Nemaha uplift as shown in Fig. 3-9. In this area, the Arbuckle surface is unconformable and locally truncated by younger formations, the base of which is Simpson Group. Another major unconformity is the Hunton rock formation. As shown in Fig.3-10, the Hunton formation is eroded, so that some Woodford formation lies on rocks as old as Simpson.

With the above understanding and the well tops picked in Section 3.2.2, A to I surface are built for A to I formation. And KB surface presents the ground surface of this reservoir. The stratigraphy of this field is then modeled.

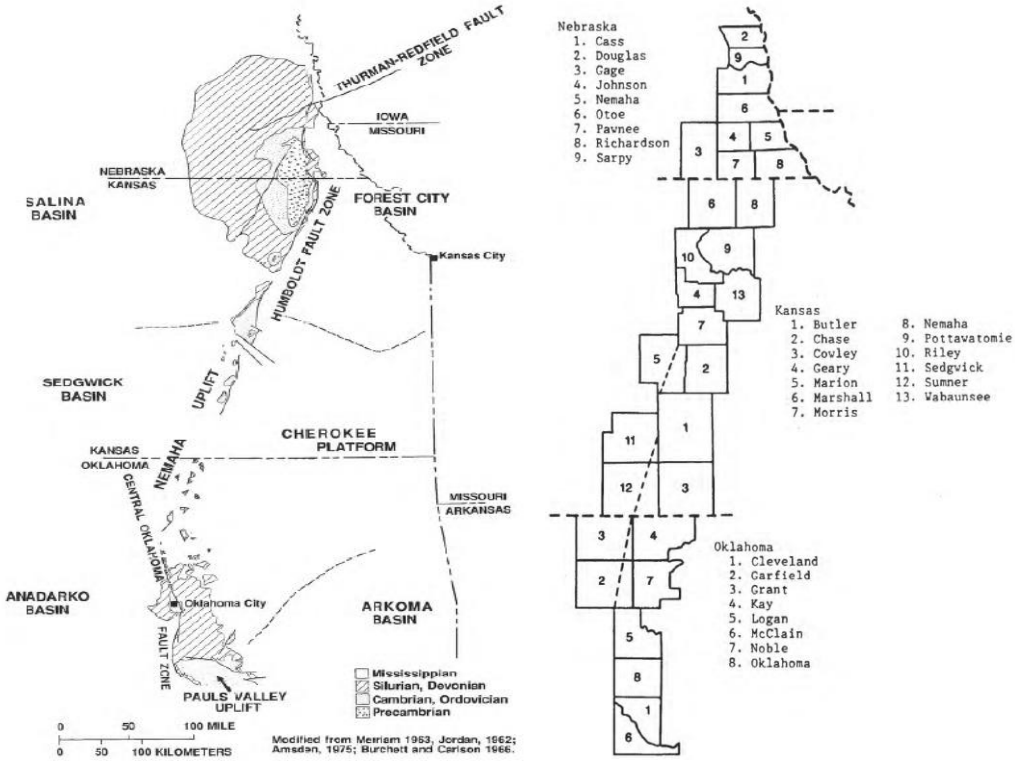

Figure 3-9 Nemaha uplift and included counties (after Dolton and Finn, 1989)

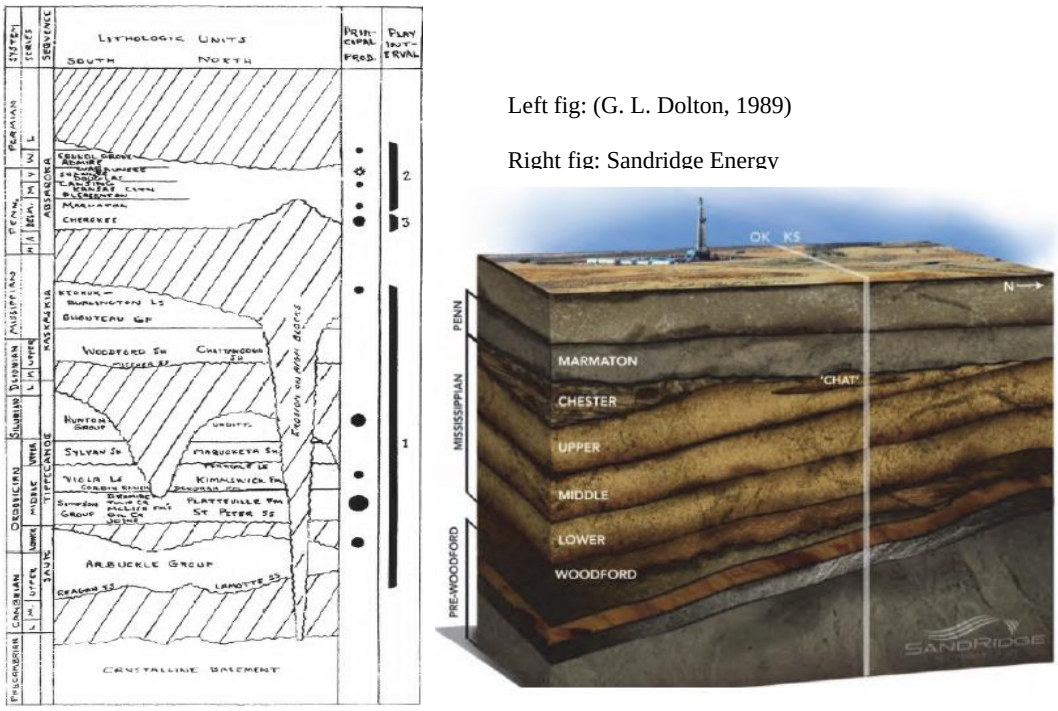

Left fig: (G. L. Dolton, 1989)

Right fig: Sandridge Energy

Figure 3-10 General correlation chart and stratigraphy

As introduced in Section 3.3, the 1D MEMs only describe the reservoir attributes along the wellbores. The surfaces can connect the same well tops and generate the MEM from 1D to 3D, so that the geological and mechanical features along each well are grouped for each formation. The grid increment of surface interpolation is set as 200 ft ×200 ft, which is in a reasonable range to capture the horizontal geological features and also to be computed in an acceptable time period. The algorithm of convergent interpolation is used to generate the surfaces in this project according to the manual of Petrel software since the primary input is with low well top density. In this project, the surfaces of I and D formations are truncated by their above surfaces, whereas other surfaces are conformable with the knowledge of reservoir stratigraphy.

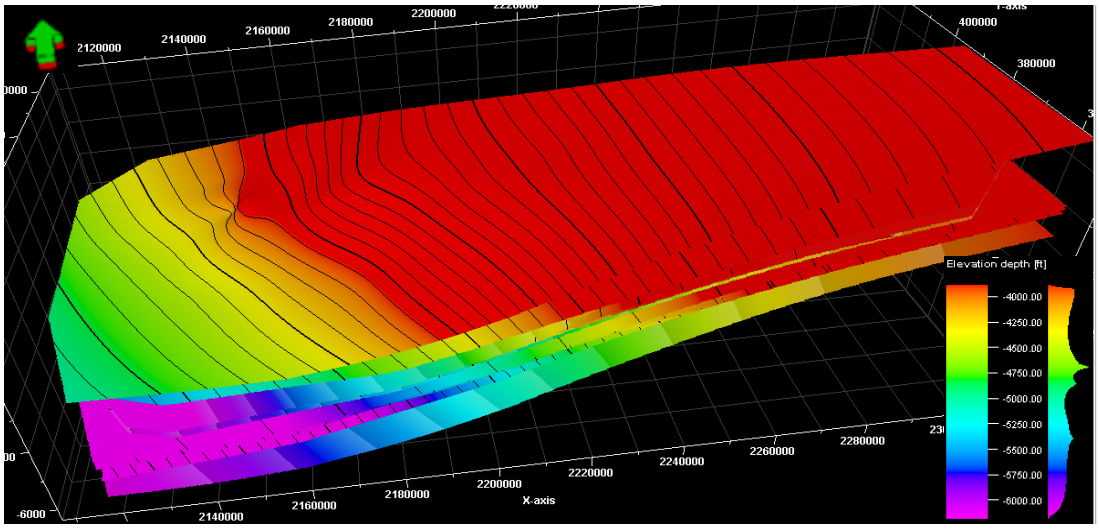

Figure 3-11 3D view of the surfaces

Necessary editing work was then conducted to remove the unsmooth peaks, which may be caused by the interpolation or singular point. Figure 3-11 shows the edited and smoothed faces.

3.5 Structural Framework

In this section, the reservoir structural framework is constructed. First, the A to I horizons are made from the A to I surfaces with their stratigraphic features (comfortable, eroded and truncated). Then reservoir zones are made basing on A to I horizons so that the volume of the 3D model is built. After that the 3D model is meshed into 3D grids. Finally, the interested facies and petrophysical properties are generated for the 3D grid cells so that the 3D MEM is constructed.

3.5.1 3D Grid Construction

In this work, 3D Pillar Grid method is used to construct the 3D grid. The polygon boundary of the 3D model as shown in Fig. 3-2 is set as the vertical boundary of the target B formation. The model vertically includes the sections from the ground surface

to the I formation surface. After the boundary set up, the grid size is set as 200 ft × 200 ft in the horizontal direction.

3.5.2 Horizons and zones making

The horizons A to I are made according to the surfaces A to I, made in Section 3.4. Then 8 zones (A to H) of the reservoir are constructed between the horizons. The zone of KB horizon to A horizon is also made for convenience to consider the formation density and further calculate the overburden stress. The zone divisions are all simplified as *proportional* to draw the cell height from the cells in the following study. The cell thickness (vertical grid size) of target zones is kept about 4-5 ft to capture the vertical geological feature, while the thickness of the other zones is set coarser (15 ft or more) to reduce the computing time. Fig. 3-12 presents the horizons and zones divisions.

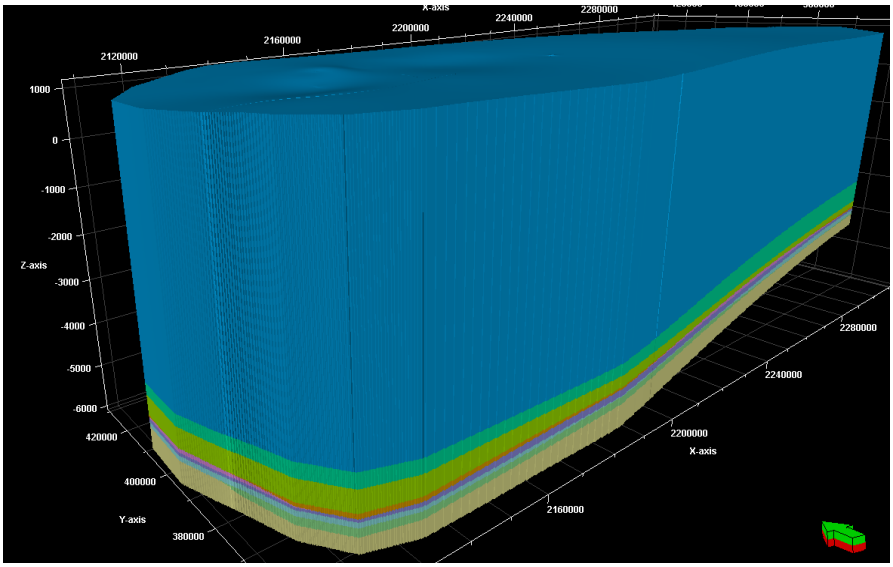

Figure 3-12 Reservoir geometry

3.5.3 Faults in the Model

The Pink lines in Fig. 3-12 gives the 2D fault map for the reservoir. Because there is no available reports showing the 3D fault shapes, types, and displacements, in this work

we adopted two methods to add faults into the model. For the reservoir portion with available seismic data as shown in the blue grids in Fig. 3-13, the 3D shapes of the faults can be added through seismic interpolation. For the rest of the reservoir that the seismic survey does not cover, the fault shapes and types are assumed.

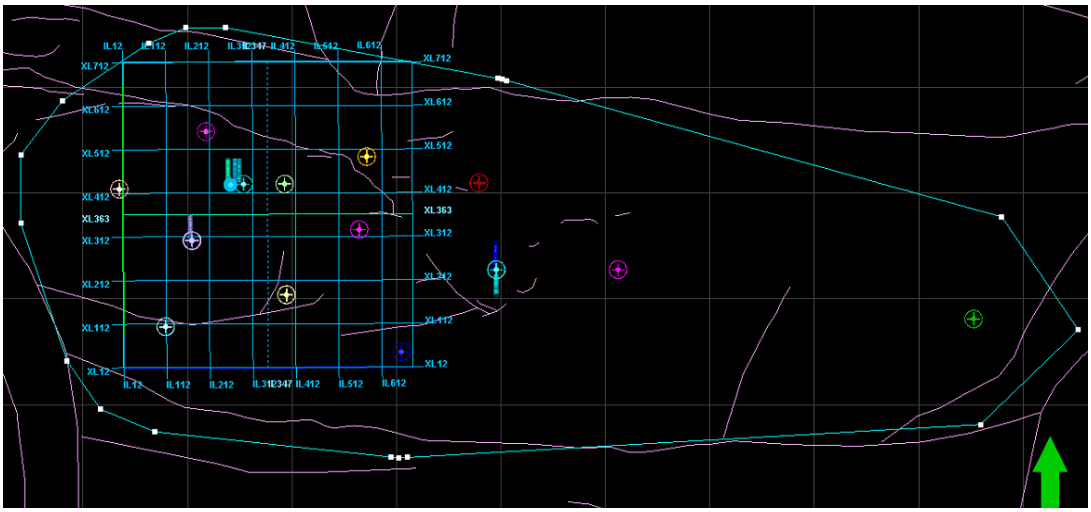

Figure 3-13 2D Faults (pink lines) and seismic data (blue grids) in the MEM

The seismic data is in the time domain, but the 3D MEM is constructed in depth domain. Therefore, the seismic needs to be tied well data. In another word, the well data measured in depth units can be compared with the seismic data measured in time units through well-seismic tie. It should be noted that there is only depth-time curve information for 3 wells, 2 of which are in the reservoir of interest. The converted seismic data are then interpreted to obtain the fault shapes through seismic interpretation with Petrel. The shapes and displacements of the faults not covered by seismic are assumed and created by the fault polygon function. The fault polygons are generated to 3D shapes according to the given 2D fault map. The fault pillars which stand for the fault surfaces are edited to ensure the input log variations are consistent

with the fault effects. Fig. 3-14 presents a 3D fault created from the fault polygons. And Fig. 3-15 plots the faults in the 3D model.

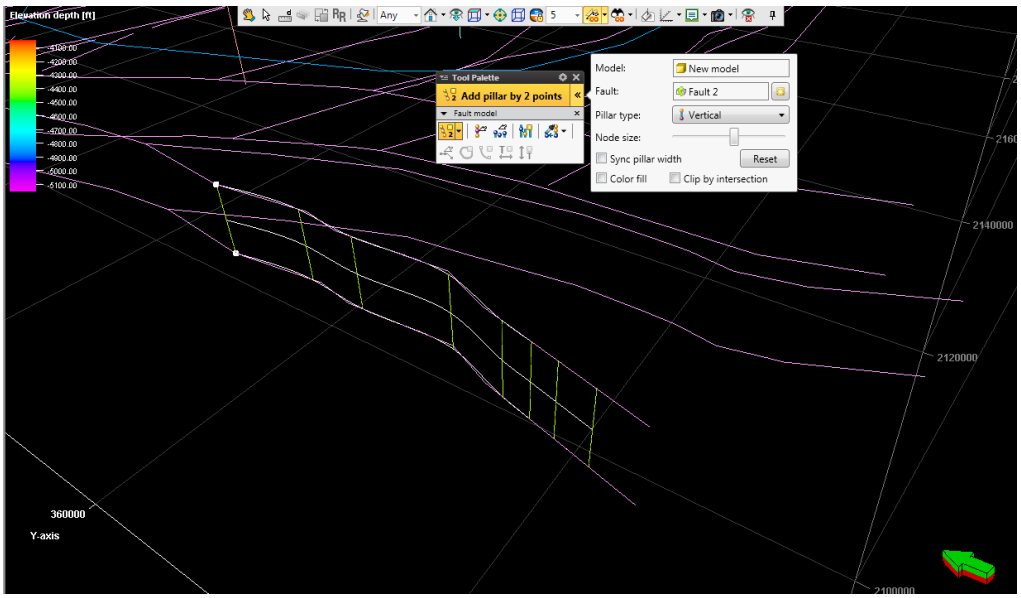

Figure 3-14 Faults created from the fault polygons

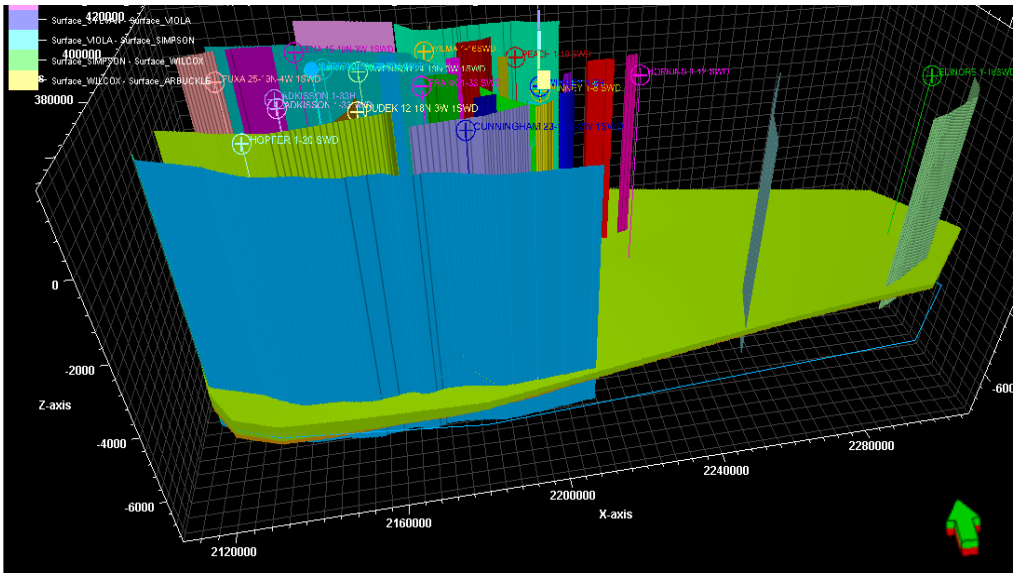

Figure 3-15 Faults in the reservoir.

However, the fault effects are not considered in the following property modeling. As so many assumptions are made for the faults shapes so that the modeled faults might not well present the reality.

3.6 Property Modeling

In this section, the properties obtained from well logs are upscaled. Because in the model, the vertical grid cell sizes are 5 ft which is much larger than the data spacing of well logs (0.5 ft or 1 ft). So, it is necessary to upscale rock properties from well log reservoir model. Facies are then created. Due to the lack of log data, data analysis is further conducted to prepare input information for further petrophysical modeling.

3.6.1 Upscaling

1) Upscale lithology logs

Discrete lithology logs are upscaled by use of the average *Most of* method. The lithology logs with the same templates are built on the basis of the lithology and mineralogy information for the wells with available information. Fig. 3-16 presents the upscaled lithology logs and original lithology logs in a well section window. Gamma ray and SP logs are also showed in Fig. 3-16 as references to identify the lithology and to compare the upscaled lithology logs. From the figure, it can be observed that the upscaled lithology logs are close to the original lithology logs and upscaled lithology logs can capture the main lithology features from the original logs. But some lithology details and variations within short depth are ignored. That is the reason why differences of lithology percentages are produced during upscaling.

Figs. 3-17 through 3-19 are the histograms comparing the data from upscaled lithology logs and original lithology well logs. The green histograms are upscaled logs and the red ones are well logs. For both upscaled histograms and well log histrograms, 0 indicates sandstone, 1 is limestone and 2 is shale. The differences of lithology

percentages are produced during upscaling, but they are corrected in the following modeling step, in which the lithology percentages of original lithology logs are fixed.

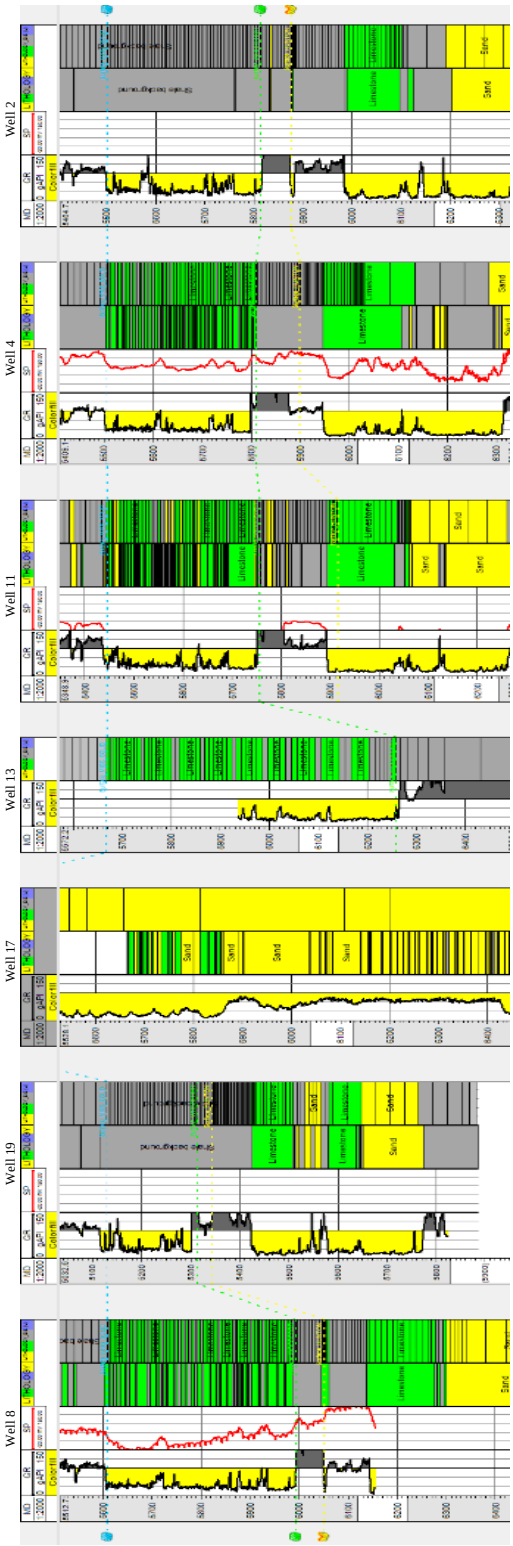

Figure 3-16 Comparing the Gamma Ray, SP, lithology and upscaled lithology logs for target B formation (Yellow is sandstone, green is limestone, gray is shale)

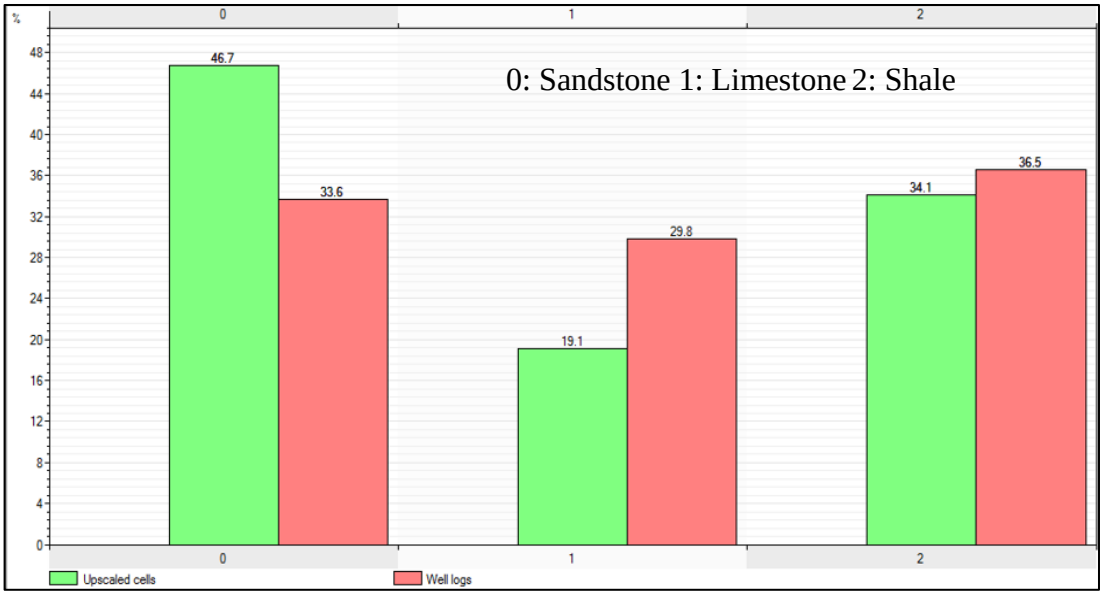

Figure 3-17 Histogram of the upscaled lithology logs for the reservoir

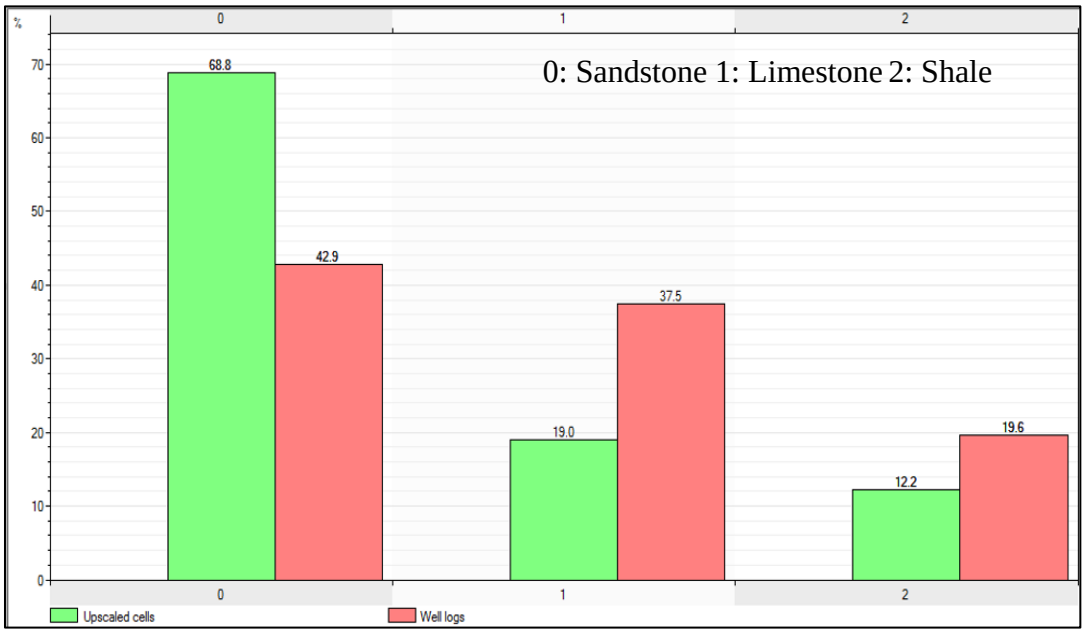

Figure 3-18 Histogram of the upscaled lithology logs for the target B formation zone

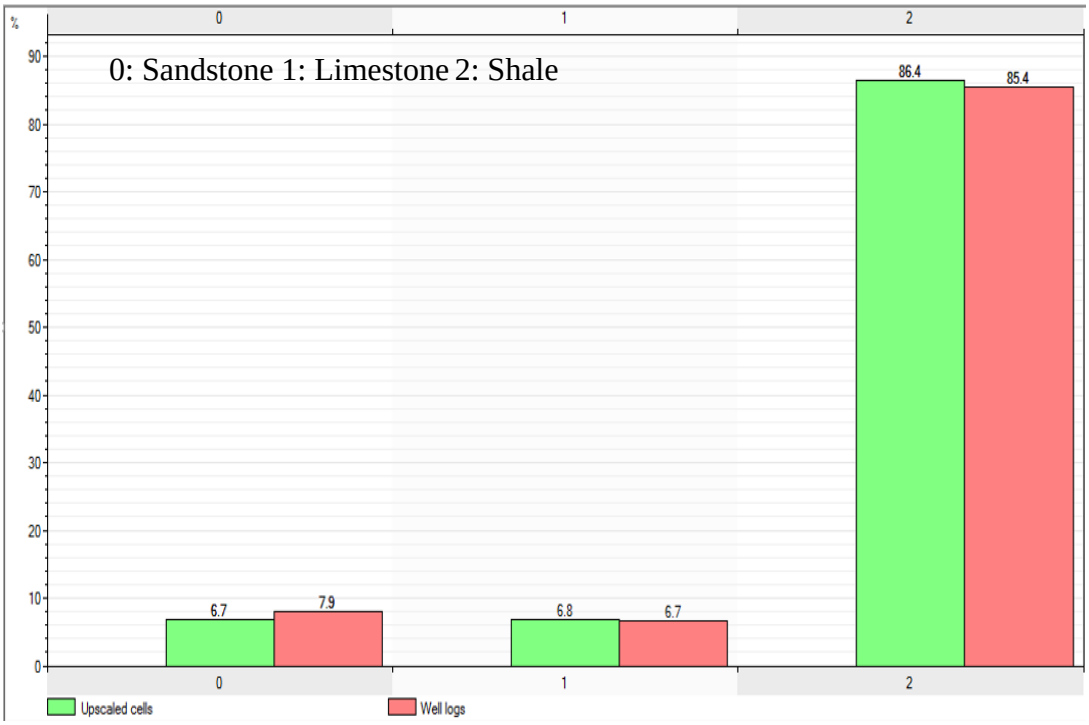

Figure 3-19 Histogram of the upscaled lithology logs for the target C formation zone

2) Upscale petrophysical logs

The petrophysical logs are considered as continuous logs, which are upscaled after facies modeling since they are influenced by the facies lithology types and the sequential indicator simulation (SIS) facies modeling results.

3.6.2 Facies Modeling

Facies modeling is to generate lithology facies from the upscaled lithology logs to the 3D model. The facies model is used as bias basis during generating the petrophysical properties in the following section. With the upscaled lithology logs of the above wells, facies modeling is conducted using the SIS algorithm, which is a stochastic modeling technique and is most appropriate for uncertain shapes of particular facies bodies. As the limestone formation diagenesis process is more complicated than sandstone sedimentary process, so that there is more uncertainty in the limestone shape body. SIS algorithm is applied to consider the heterogeneity of the facies in both B limestone formation and C shale formation. Figs. 3-20 and 3-21 present the facies modeling results of B limestone formation and C shale formation, respectively.

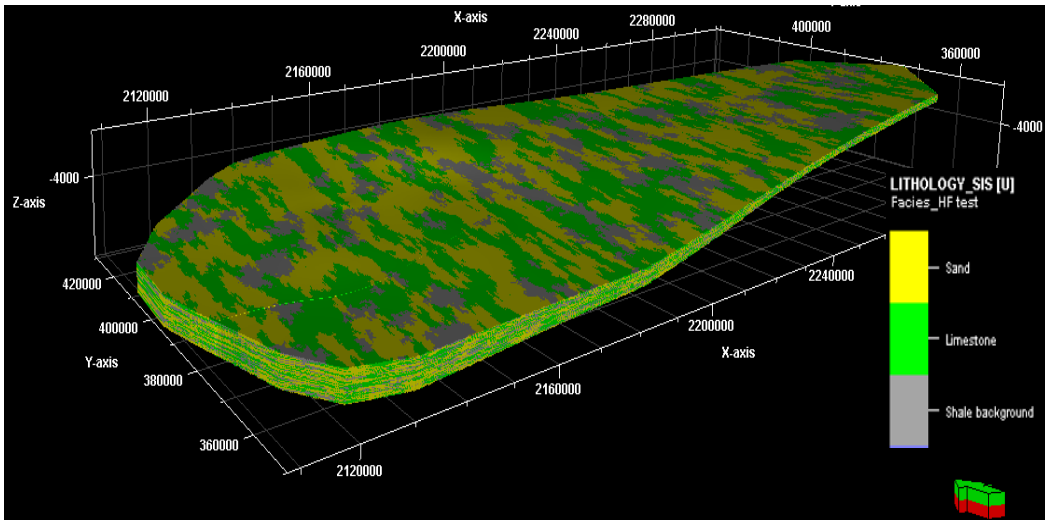

Figure 3-20 3D view of the facies in B limestone formation

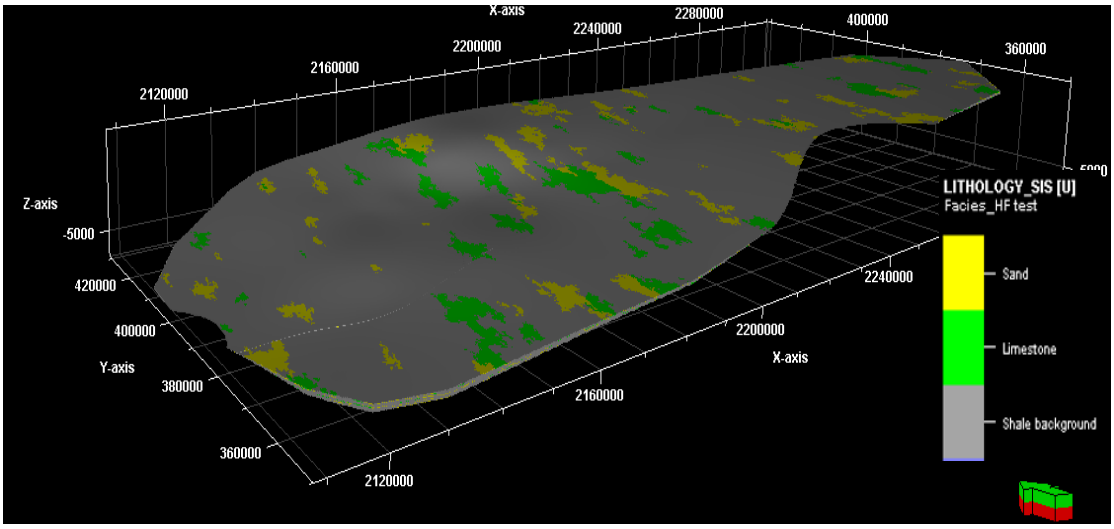

Figure 3-21 3D view of the facies of C shale formation

3.6.3 Data Analysis

Data analysis is a preprocessing step for using Sequential Gaussian simulation algorithm in petrophysical modeling, which requires normalized data and a variogram range. The variogram range is also useful for the Kriging algorithm to take account into the anisotropy range. In this project, the upscaled petrophysical logs are analyzed for every lithology in each zone. The vertical, major and minor directions and anisotropy ranges are adjusted for the variogram computations. Fig. 3-22 presents an example of data analysis of density for limestone formation in B formation zone, showing the distribution of density values and the variation in different directions.

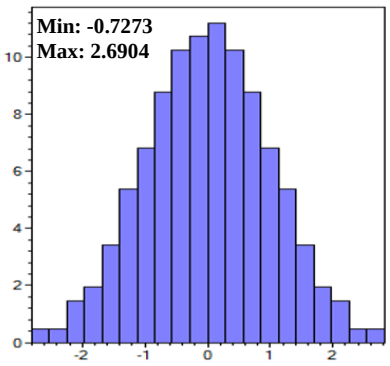

a) Transformations with Normal score distribution

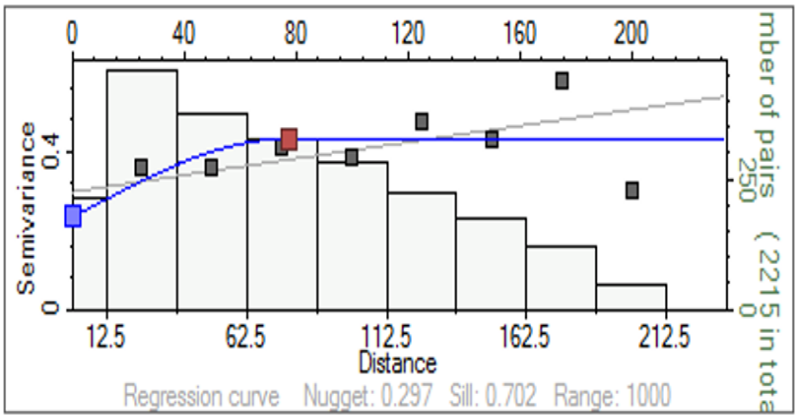

Major range: 500 Minor range: 500 Vertical range: 77.627

(b) Variograms

Figure 3-22 Data analysis of density for limestone formation in B formation zone

3.6.4 Petrophysical Modeling

Petrophysical modeling is a step to generate the properties from the upscaled property logs (in section 3.3.3-1) on the bias of lithology facies (section 3.3.3-2) at each position to the 3D reservoir. It is conducted with the data preprocessed by *Data analysis.* Petrophysical modeling in this project is interpolated with two algorithms: Sequential Gaussian simulation (SGS) and Kriging. SGS which is one of the most common algorithms is a stochastic simulation method honoring well data, input distributions, variograms, and trends. It gives different representations from each calculation and offers the possibility and uncertainty of the property distribution. Kriging, a deterministic simulation method, is an estimation technique that uses a variogram to express the spatial variability of the input data. The results from these two algorithms are compared with each other. Formation density and Young's modulus models for the target B formation are shown below in Figs. 3-23 and 3-24.

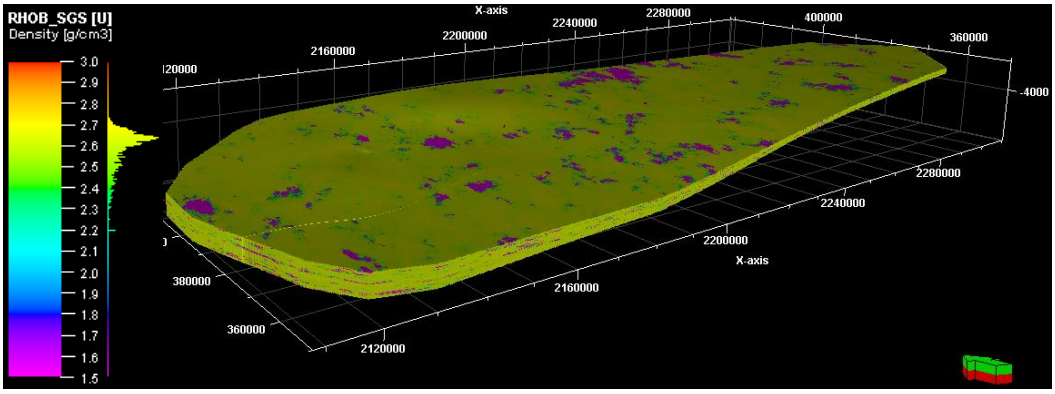

a) SGS algorithm

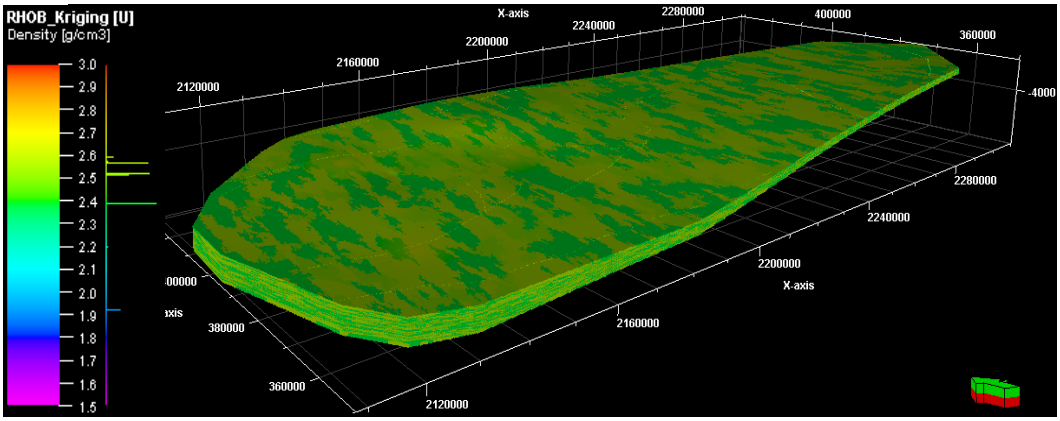

b) Kriging algorithm

Figure 3-23 Formation density from SGS and Kriging algorithms in B limestone formation

By comparing the two figures in Fig. 3-23, the formation density model calculated from the SGS algorithm is slightly higher than Kriging algorithm, and it is more heterogeneous from SGS. The formation density model from SGS is closer to the upscaled logs and the original logs, indicating the formation density model from SGS algorithm better presents the reservoir density than the Kriging algorithm.

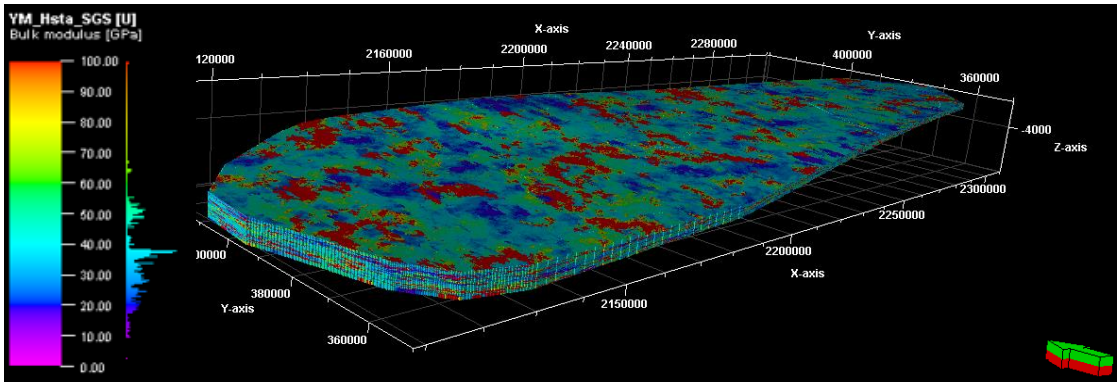

a) SGS algorithm

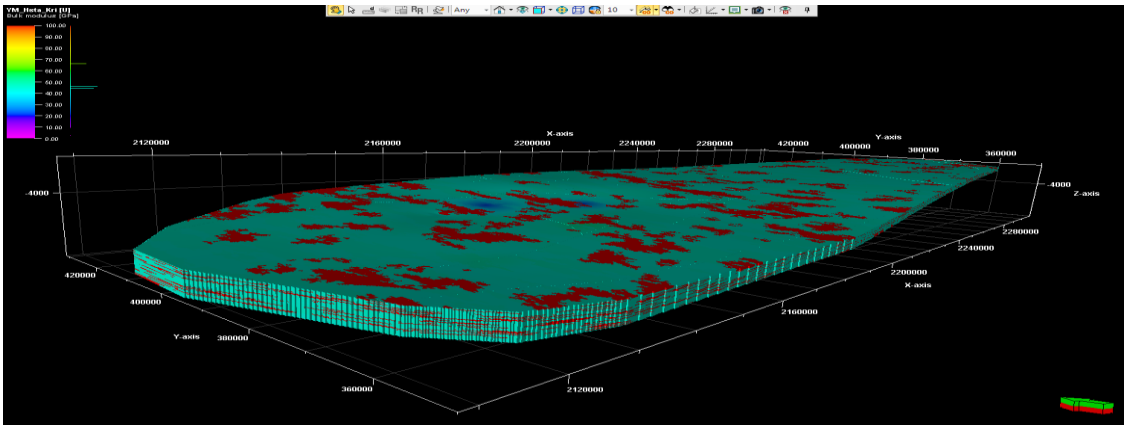

b) Kriging algorithm

Figure 3-24 Young's Modulus from SGS and Kriging algorithms in B limestone formation

Figure 3-24 indicates the major ranges of the Young's modulus models of B formation from the two algorithms are close to each other. But similar to the formation density model, the SGS models carry more heterogeneity than Kriging models. And there are locations in the SGS model show high and low Young's modulus values as in the original well logs, but this information is omitted in the Kriging model. Therefore, the SGS model gives more reasonable results and is adopted in the MEM construction.

3.6.5 Stress Modeling

The stress model is calculated with the same equations in the 1D MEM in-situ stress calculation. The overburden stress model is calculated from the integration of formation density model with depth (Eq. 3-1). Then the minimum horizontal stress model is calculated from the Young's modulus, Poisson's ratio and pore pressure models (Eq. 3-20). In shale formation, the calculated in-situ stress is anisotropic since the rock properties in shale are anisotropic. The models of formation density, Young's modulus, Poisson's ratio and pore pressure are carrying the heterogeneity so that the in-situ stresses calculated from the models are also heterogeneous. Then magnitudes of the in-situ stresses are calibrated with hydraulic fracturing (HF) pressure data and the directions of these stresses are calibrated with HF fracture shapes from microseismic measurements and the breakouts and drilling-induced fracture orientations. The HF operation pressure data is available for Well 17 and Well 18. Fig. 3-25 show the directions of the horizontal portion of these two wells. The axis of these two wells are on the direction of the minimum horizontal stress, and the vertical stress and maximum horizontal in-situ stresses are in the plane of wellbore cross sections, as shown in Fig. 3-26.

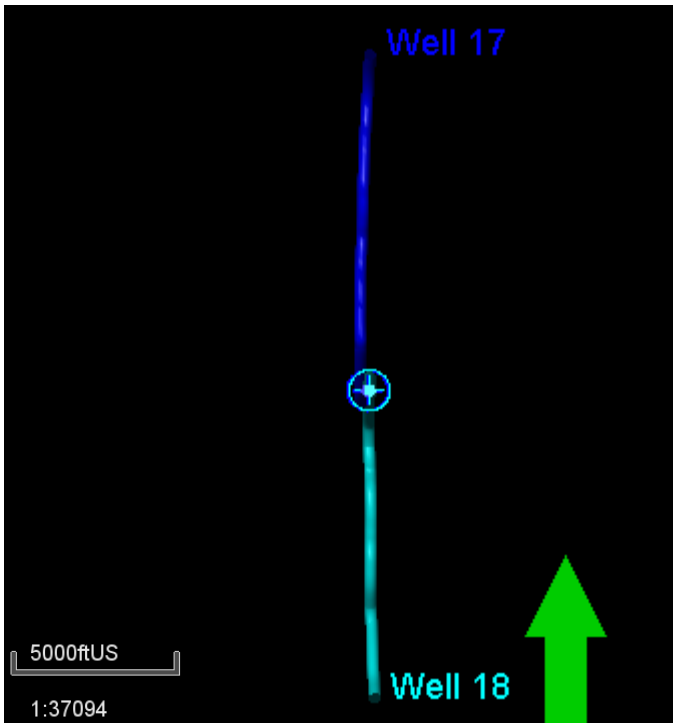

Figure 3-25 Well 17 and Well 18 in bird view

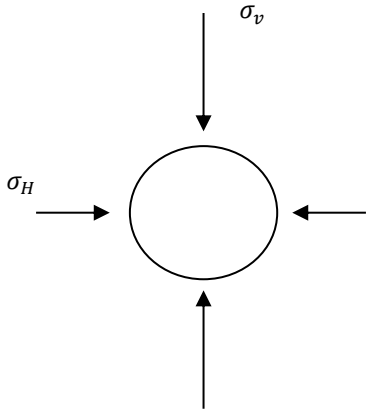

Figure 3-26 Wellbore cross section of a horizontal portion (in North/South side view)

Take Well 18 as an example to illustrate the in-situ stress calibration process using the HF data. In Well 18, the HF is operated in the horizontal portion, which is at 5672 - 10016 ft in MD (about 5176.28 - 5225.65 ft in TVD) in B formation. The breakdown

pressure and final ISIP (at well head) are listed in Table 3-3, according to the HF operating pressure data.

Table 3-3 Breakdown and ISIP of Well 18

Stage	Top MD, ft	Bottom MD, ft	Breakdown pressure. Psi	Final ISIP, Psi
1	9698	9952	7385	1069
2	9363	9616	2928	885
3	9027	9281	6013	932
4	8692	8945	3960	890
5	8356	8610	7503	969
6	8021	8274	6555	1059
7	7685	7939	2702	1077
8	7350	7603	7285	919
9	7014	7268	6108	1020
10	6679	6932	2511	1050
11	6343	6597	2323	1060
12	6008	6261	3984	1102
13	5672	5926		1110

To estimate the in-situ stresses, ISIP at well head is first transferred to operating depth according Eq. 3-22.

$$P_b = P_b^{wellhead} + \rho_{mud} * g * h^{TVD}$$
$$ISIP = ISIP^{wellhead} + \rho_{mud} * g * h^{TVD} \quad (3\text{-}22)$$

The horizontal portion of the Well 18 is drilled in the north-south direction, which is the same as or close to the minimum horizontal in-situ stress. So the ISIP represents the minimum horizontal stress. The vertical stress can be estimated from Pine et al. (1983)

$$\sigma_v = 2\sigma_h - P_b + T \quad (3\text{-}23)$$

Then maximum horizontal stress is estimated from the minimum horizontal stress using the Eq. 3-21. Therefore, the in-situ stress from the Well 18 HF data, shown in

Table 3-4, is compared with in-situ stress in the 3D MEM. Then the in-situ stress models in the 3D MEM are calibrated.

Table 3-4 In situ stress of Well 18 from the HF pressure data

Stage	Top MD, ft	Bottom MD, ft	Min horizontal in-situ stress, psi	Max horizontal in-situ stress, psi	Vertical in-situ stress, psi
1	9698	9952	3150	3244.5	3311.568
2	9363	9616	3155	3249.65	7652.099
3	9027	9281	3191	3286.73	5092.764
4	8692	8945	3153	3247.59	6606.996
5	8356	8610	3230	3326.9	7613.363
6	8021	8274	3314	3413.42	4502.099
7	7685	7939	3328	3427.84	7102.434
8	7350	7603	3170	3265.1	3343.434
9	7014	7268	3249	3346.47	4759.968
10	6679	6932	3298	3396.94	5061.062
11	6343	6597	3312	3411.36	8730.167
12	6008	6261	3354	3454.62	7196.9
13	5672	5926	3360	3460.8	9139.134

The borehole image logs are available for Well 2, Well 7 and Well 13. The drilling-induced fractures and breakouts can be identified in the borehole image logs. The maximum and minimum horizontal stress directions are estimated and calibrated based on the drilling-induced fracture and breakouts directions from the borehole image logs. The calibration detail is shown in the case study in Section 4.1.

Microseismic measurements of hydraulic fractures are available for Well 12, Well 13 and Well 15. The directions of the minimum and maximum horizontal in-situ stresses are calibrated according to the hydraulic fracture directions from the microseismic measurements. The calibration detail is shown in Section 4.2 together with a hydraulic fracturing modeling case study.

The in-situ stress models are shown below, from Fig. 3-27 to 3-29.

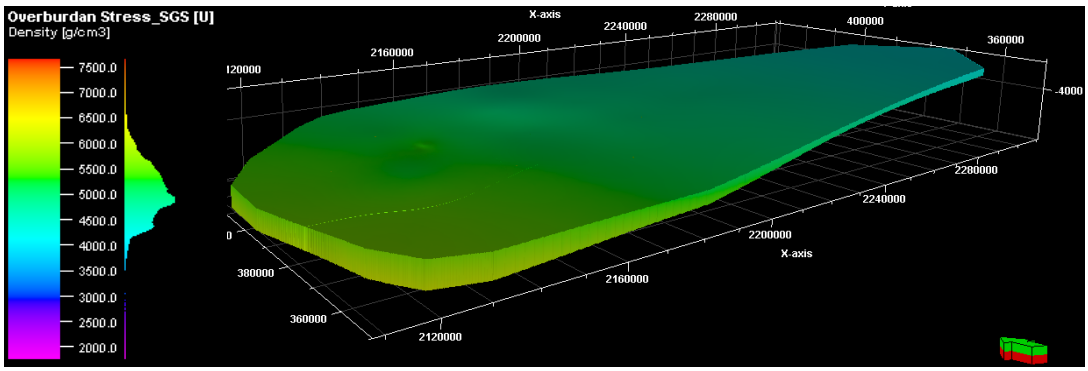

a) SGS algorithm

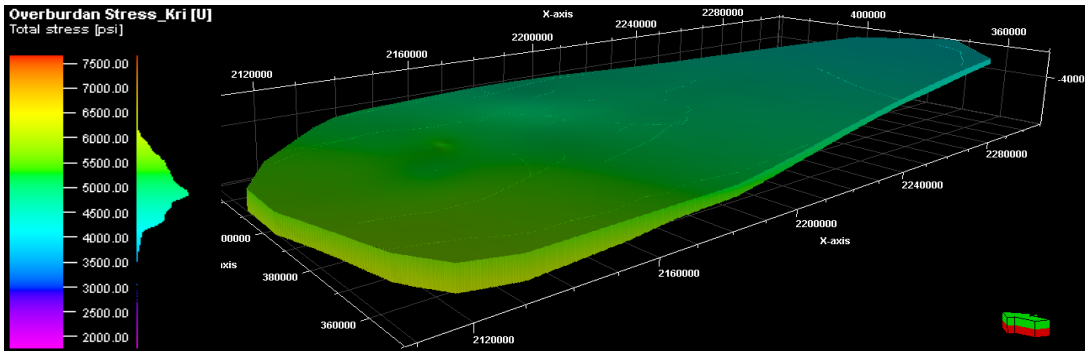

b) Kriging algorithm

Figure 3-27 Overburden stress from SGS and Kriging algorithms in B formation

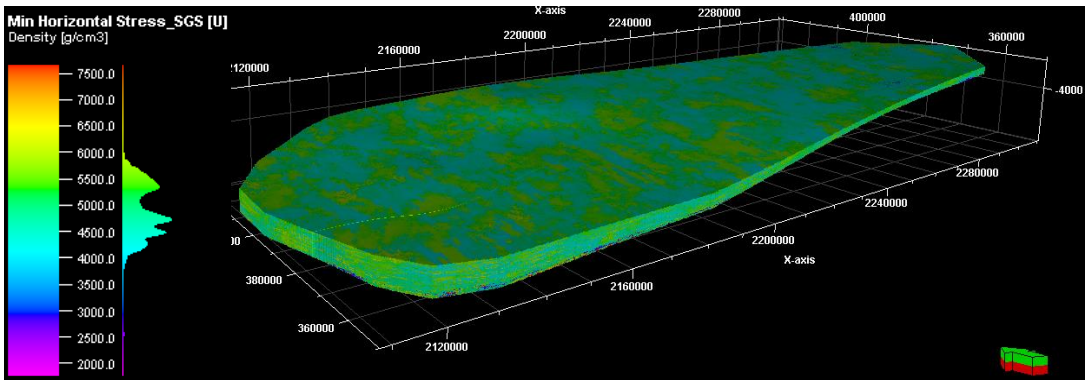

a) SGS algorithm

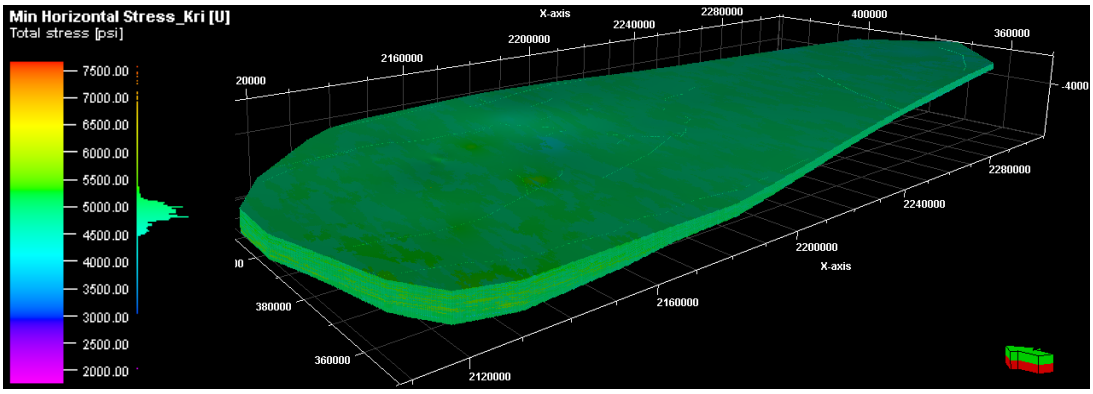

b) Kriging algorithm

Figure 3-28 Minimum horizontal stress from SGS and Kriging algorithms in B limestone formation

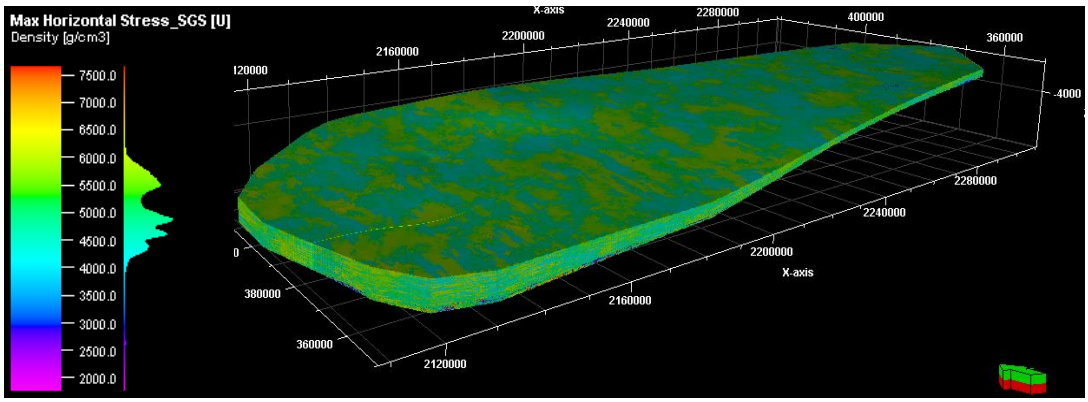

a) SGS algorithm

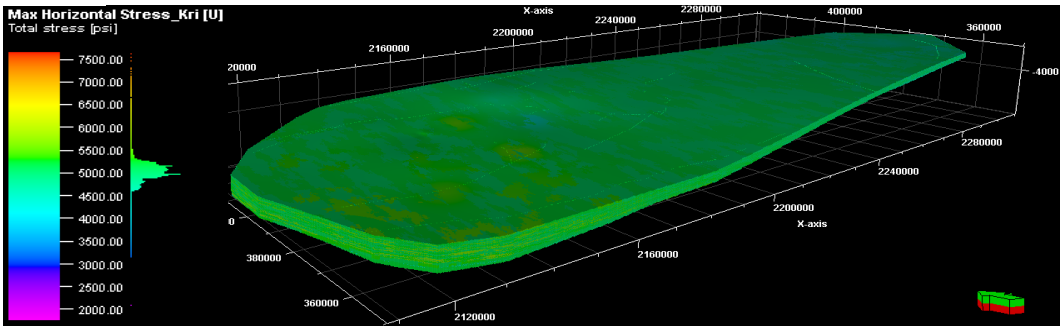

b) Kriging algorithm

Figure 3-29 Minimum horizontal stress from SGS and Kriging algorithms in B limestone formation

3.6.6 Fracture Modeling

Discrete fracture network is modeled for the B limestone and C shale formations of this filed. The procedure is summarized as below:

1) Import and display of the fracture data
2) Fracture attribute data management
3) Initial data analysis
4) Fracture parameters
5) Build the fracture model

The initial fracture data is from the borehole image logs of Well 2 and Well 7. Four types of fractures are presented in the borehole image logs: partial fractures, closed fractures, open fracture, and drilling-induced fractures, as shown in Fig. 3-29. It can be observed that the natural fractures in the reservoir are mainly closed fractures and partial fractures. The fractures are not always perpendicular to the minimum horizontal stress directions from the borehole image logs, because they might be produced by the uplift which involves more complicated stress statuses. In this 3D MEM, partial fractures and closed fractures are generated as discrete fracture network, however, the open fracture and drilling induced fractures are not included. Because only one open fracture is detected in the interested zones, it is too random to generate such a fracture. . The drilling induced fractures are used to analyze the in-situ stress status.

Well 2

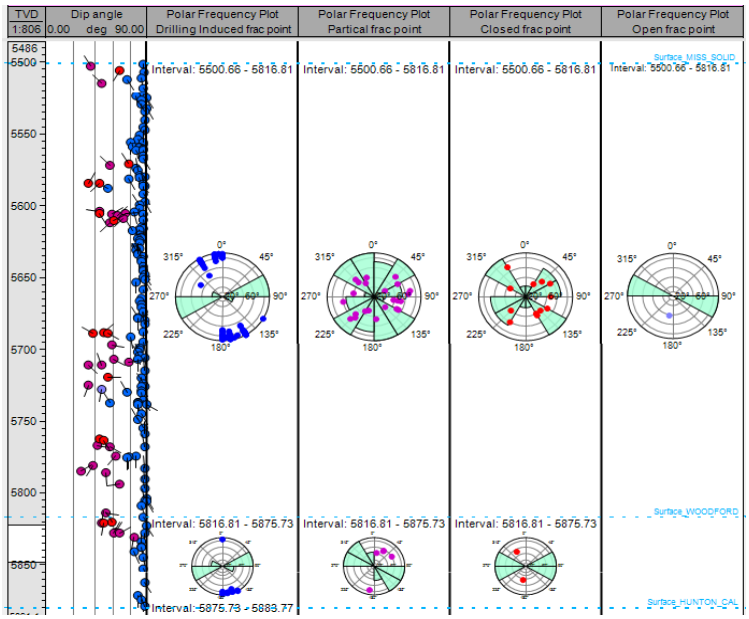

a) Initial fracture dip and azimuth of Well 2

Well 7

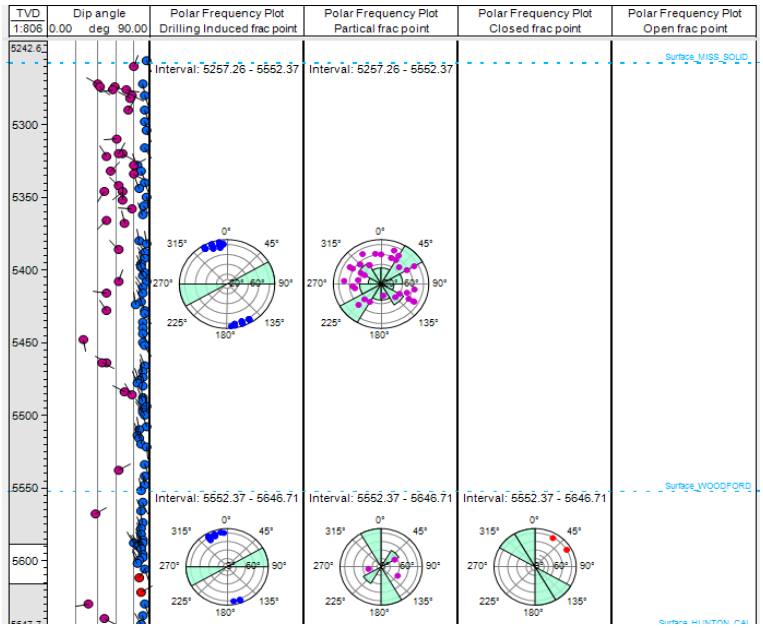

b) Initial fracture dip and azimuth of Well 7

Figure 3-30 Initial fracture dip and azimuth in B and C formations (Pink: partial fractures; Red: closed fractures; Blue: drilling induced fractures; Purple: open fracture)

Fig. 3-30 shows the initial fracture dip and azimuth in B and C formations. It can be observed that the dips of drilling-induced fracture of both Well 2 and Well 7 are about 90°, the azimuths are about 345° and 165° in both B formation and C formation. The azimuths of partial fractures and closed fractures in both Well 2 and Well 7 are from 0° to 360° in B formation without a clear trend. The dips of partial fractures in Well 2 are slightly lower than those in Well 7. Closed fractures are not presented in B formation in Well 7. The fracture densities in the B formation are larger than those in C formation. One open fracture is presented in B formation in Well 2.

Different fracture sets are defined as shown in Figs. 3-31 and 3-32 in order to be modeled with individual parameters. The following figures show the fracture sets of partial fractures and closed fractures in stereonets. From the stereonets of the original fracture data, the anisotropy coefficients and models can be determined. The partial fracture distributions of set 2 and 3 are more elliptical, indicating they are more anisotropic. The fracture set 0 and 1 are more anisotropic in closed fracture.

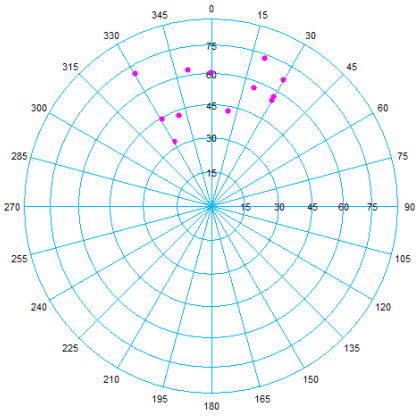

a) Fracture set 0

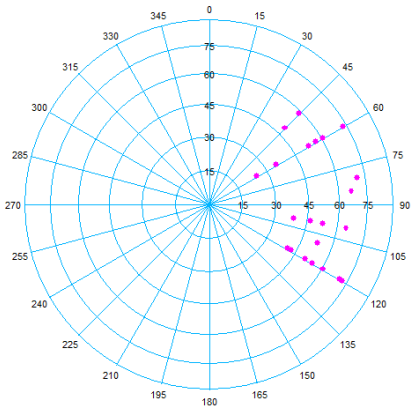

b) Fracture set 1

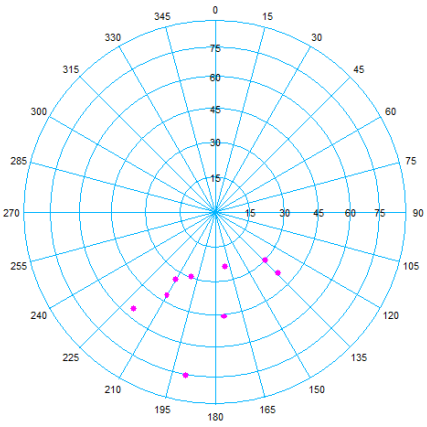

c) Fracture set 2

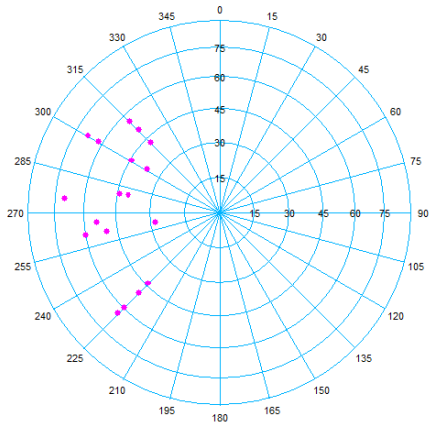

d) Fracture set 3

Figure 3-31 Fracture sets of original partial fractures in stereonet.

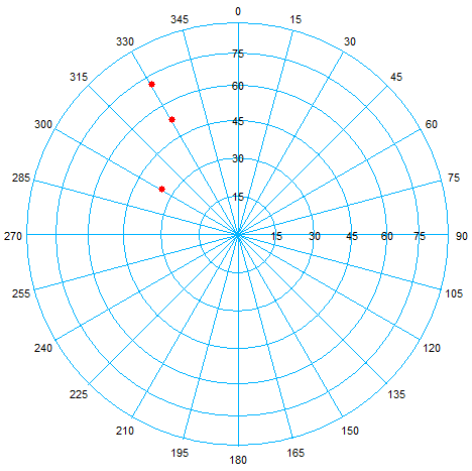

a) Fracture set 0

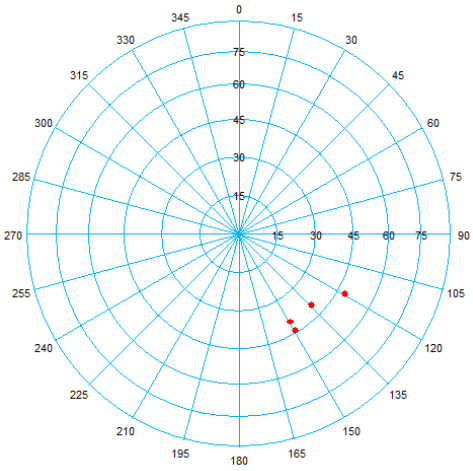

b) Fracture set 1

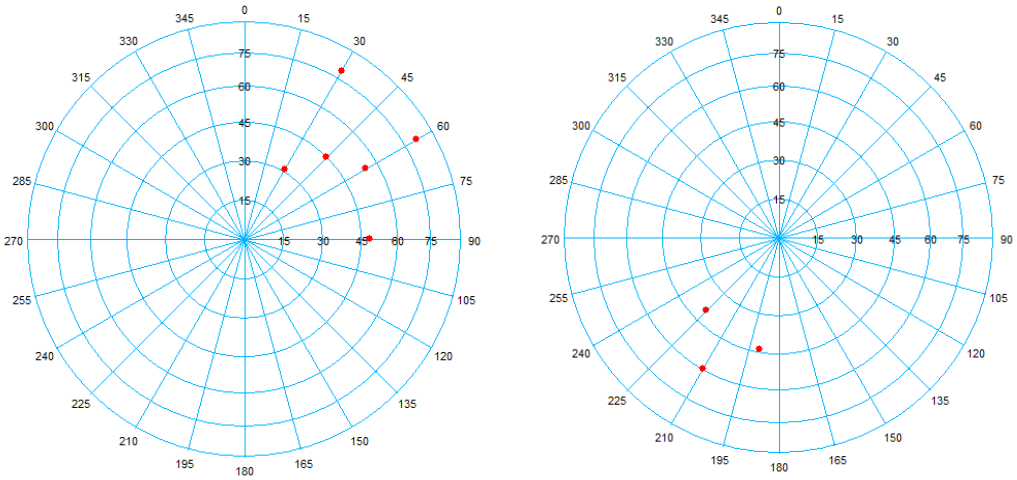

c) Fracture set 2 d) Fracture set 3

Figure 3-32 Fracture sets of original closed fractures in stereonet

The intensity logs and cumulative fracture count logs are created for the different fracture sets, and then the intensity logs and cumulative fracture count logs are used to calculate the 2D fracture density maps and 3D fracture density properties. In this project, the Sequential Gaussian simulation method is used to populate the fracture intensity because of the low original data density. The intensity property of fractures is shown in Fig. 3-33.

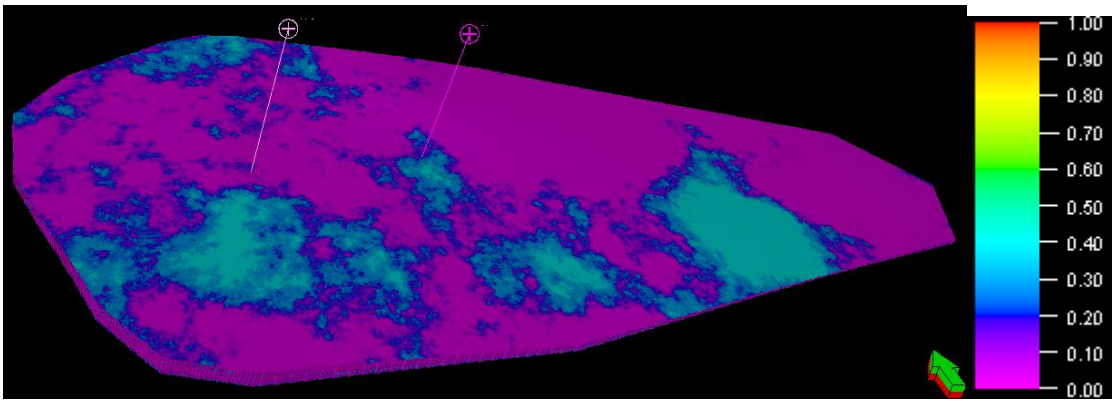

a) Fracture set 0

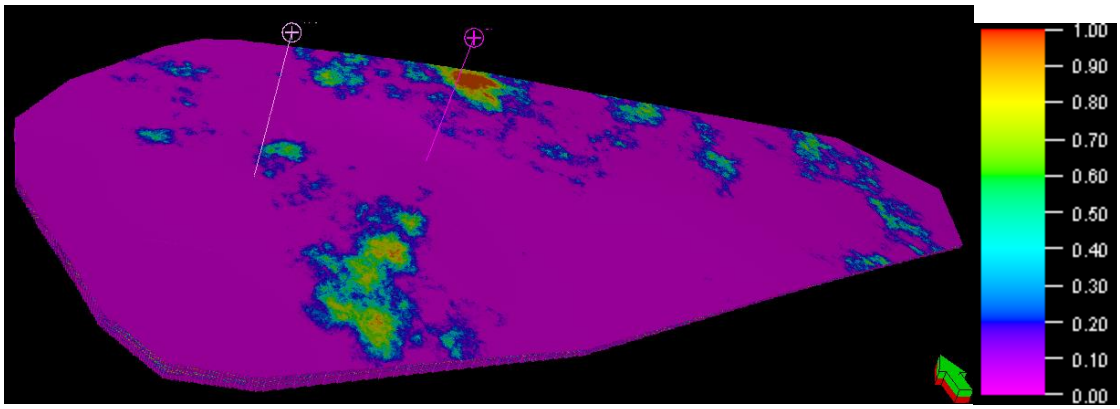

b) Fracture set 1

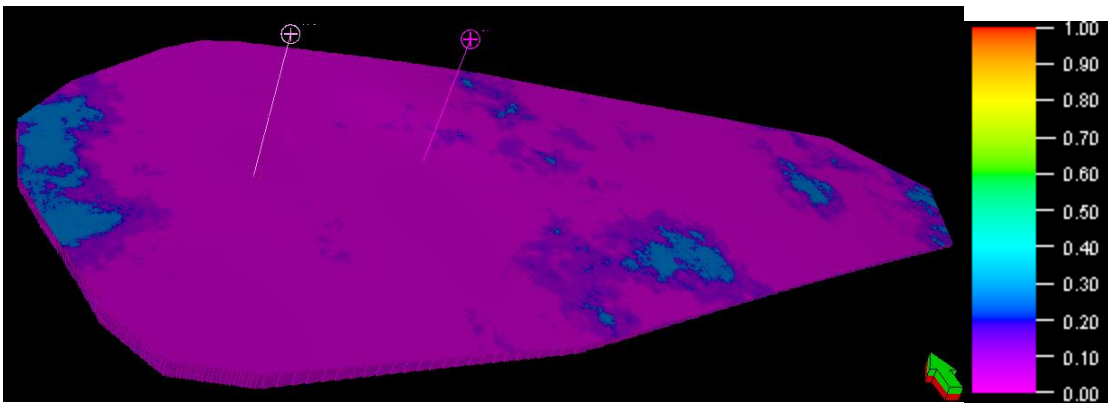

c) Fracture set 2

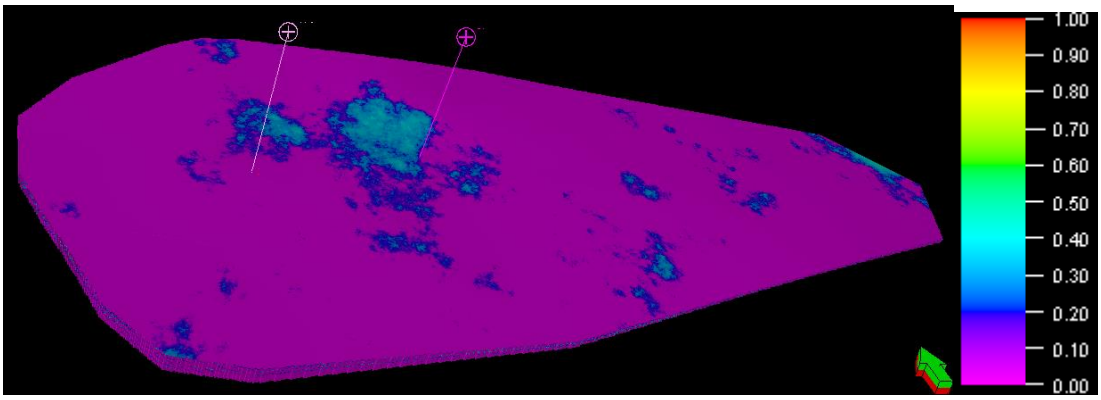

d) Fracture set 3

Figure 3-33 Partial fracture intensity property in 3D window.

Fig. 3-33 plots the partial fracture intensity property for each fracture set in the 3D model. The fracture set 0 with fractures azimuth ranging 330°-30° shows in a wide area

with intensity of 0.4, while the fracture set 1 with fractures azimuth ranging 45°-120° shows high intensity in few spots in the reservoir. The fracture set 2 with azimuth ranging 135°-225° and fracture set 3 with azimuth ranging 225°-315° cover relatively small area in this case.

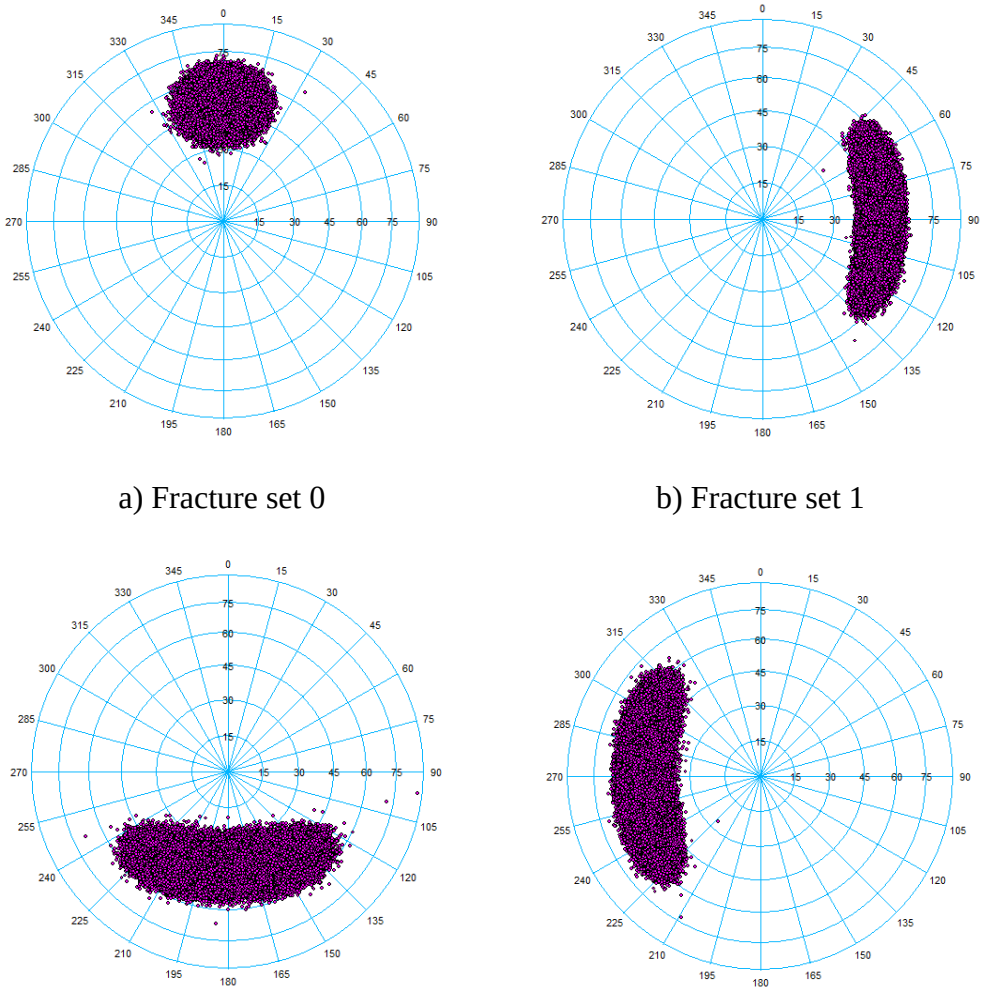

a) Fracture set 0

b) Fracture set 1

c) Fracture set 2

d) Fracture set 3

Figure 3-34 Fracture sets of modeled partial fractures in stereonet

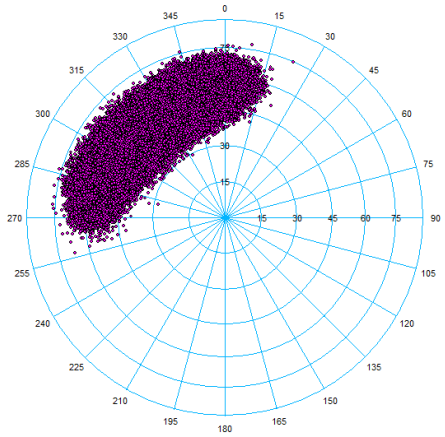

a) Fracture set 0

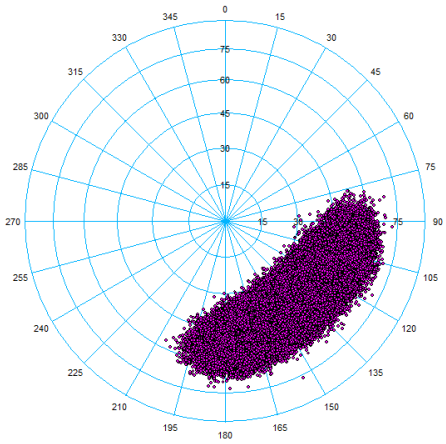

b) Fracture set 1

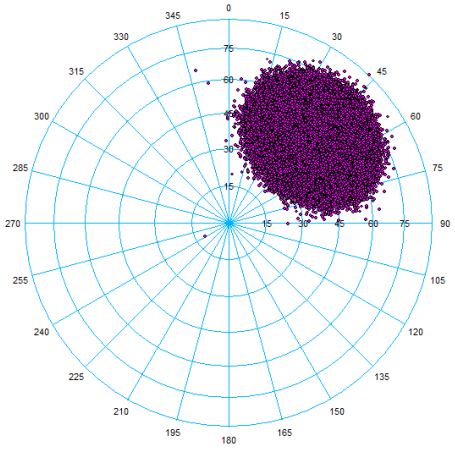

c) Fracture set 2

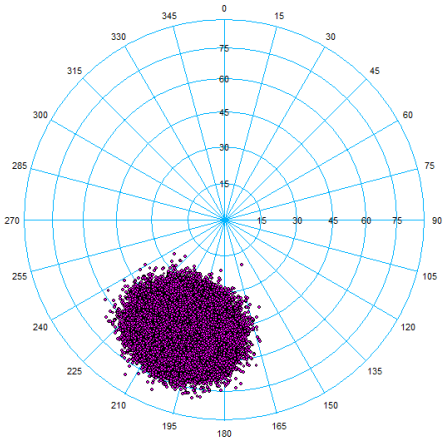

d) Fracture set 3

Figure 3-35 Fracture sets of modeled closed fractures in stereonet

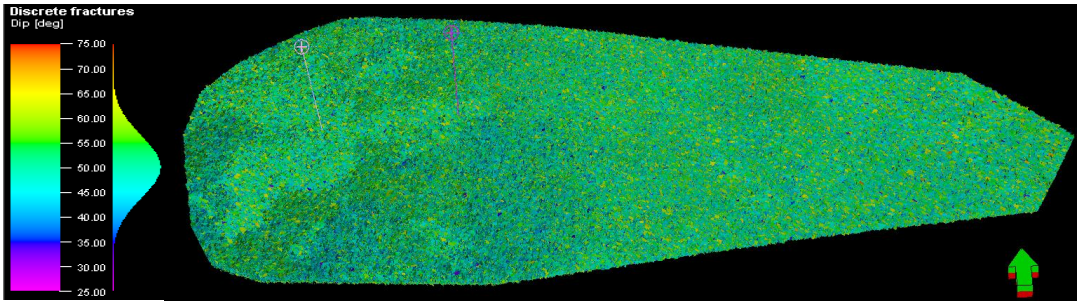

Figure 3-36 Discrete fractures dips of modeled closed fractures

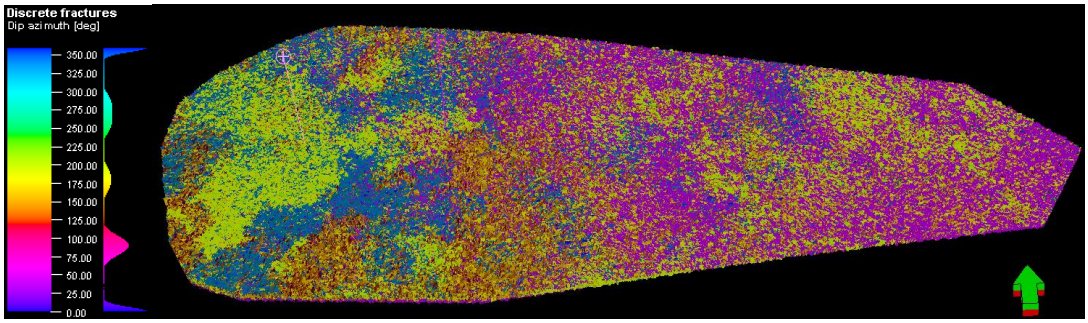

Figure 3-37 Discrete fractures dip azimuth of modeled closed fractures

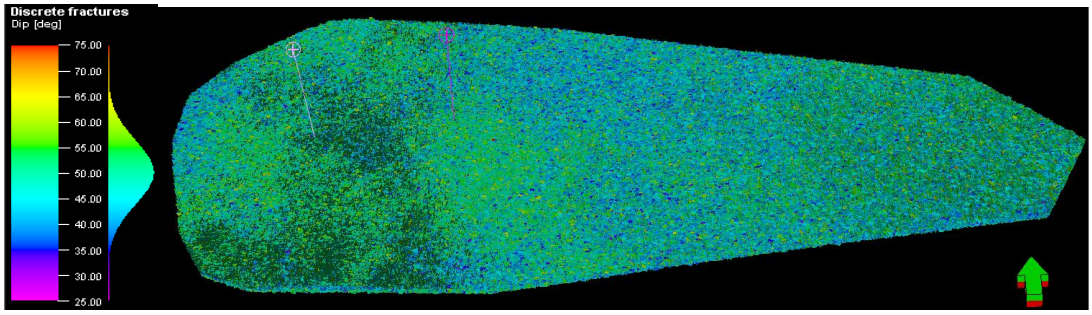

Figure 3-38 Discrete fractures dips of modeled partial fractures

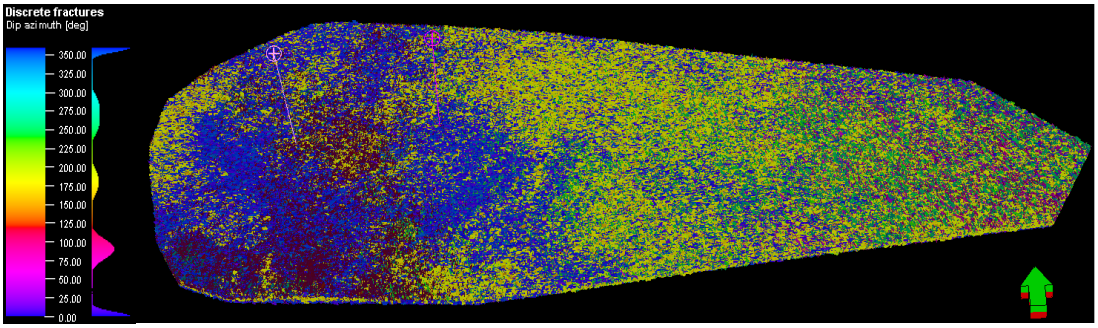

Figure 3-39 Discrete fractures dip azimuth of modeled partial fractures

The partial fractures and closed fractures are then generated basing on the fracture intensity property model. The modeled partial and closed fracture sets are shown in Figs. 3-34 and 3-35. The dips and azimuths of the modeled discrete partial fractures and closed fractures in the 3D model are shown in the Figs. 3-36 to 3-39. The primary fracture dips of the modeled discrete partial fractures (45°-55°) are lower than the closed fractures (50°-60°). The west part of the reservoir, where has relatively high well

density, has more partial fractures around 0°, whereas many 0° and 180° closed fractures are observed in this area.

3.6.7 Sector Model

A sector model of the horizontal Well 12 is cut from the above 3D MEM. This sector model carries all the properties calculated from the reservoir model. Local grids are refined in this mode to generate smaller grid blocks with i×j of 10 ft×10 ft, which is much smaller than that in the whole 3D MEM with i×j of 200 ft×200 ft. This sector model with finer grid is prepared for the hydraulic fracturing modeling in the following section. It can also provide parameters for other reservoir simulation softwares, which require detailed rock properties in the near wellbore. The following figure shows the sector model.

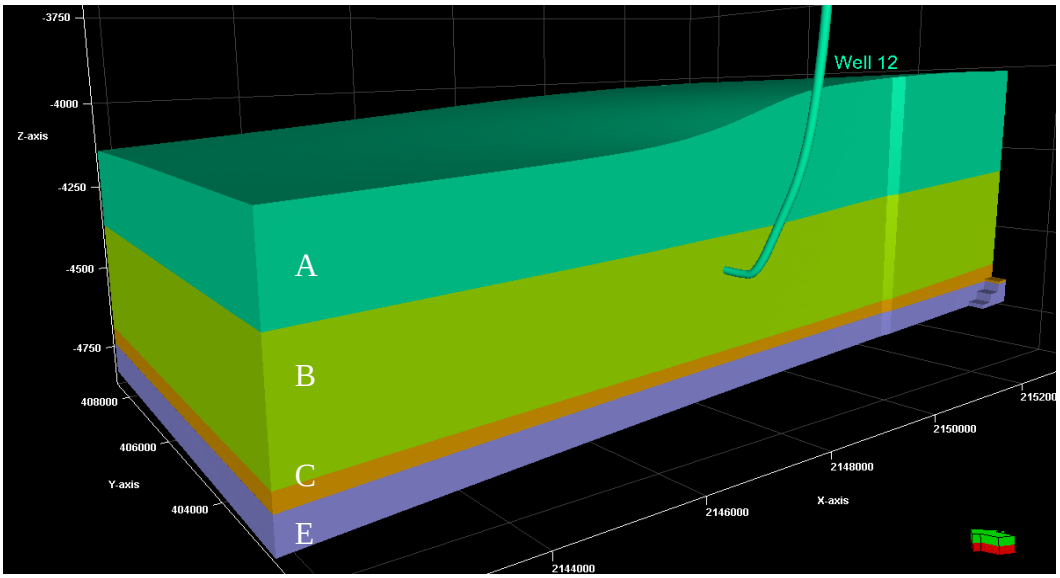

Figure 3-40 The geometry of the sector model

Chapter 4 Case Study with 3D Mechanical Earth Model

In this section, the cases of wellbore stability analysis and hydraulic fracturing (HF) simulation are performed with the input from the 3D MEM. The 3D MEM provides the parameters of the reservoir, which describes a most representative reservoir geomechanical conditions. In the cases of wellbore stability analysis, both breakouts and drilling-induced tensile cracks are available for the well 2, 7 and 13 as shown in Table 3-1. The breakouts and tensile cracks are analyzed using a finite element method (FEM) program, results from which are used to compare with the borehole image logs with the aim to verify and calibrate the 3D MEM. The HF simulation is modeled in StimPlan software to optimize the injection rate to control the length of the hydraulic fractures in target reservoir zones.

4.1 Wellbore Breakouts Analysis

In this case, the stress conditions around the wellbore of the vertical Well 2 are modeled with a FEM program using the reservoir condition inputs from the 3D MEM. The tangential Terzaghi's effective stresses around the wellbore are computed and analyzed in order to identify breakouts and breakdowns and their positions (Lu, 2013). The results of the breakouts and breakdowns are then compared with the borehole image log of Well 2, in order to verify the in-situ stresses obtained from the 3D MEM. If the results are not in good agreement with the borehole image log, the in-situ stress, in particular the maximum horizontal stress is adjusted in the FEM program to match the borehole image log. The reason is that the coefficient of relationship between the maximum and minimum horizontal stress in Eq. 3-21 is assumed. The matched in-situ

stress is then put in the MEM, and the verified or calibrated 3D MEM can be used for further applications.

4.1.1 Problem statement

Well 2 is a vertical well with available borehole image log (shown in Table 3-1). In the target B formation zone, there are two drilling-induced fractures at the depth of 5547.5 ft of Well 2 in the east-west direction, shown in Fig 4-5. And from the Fig 4-5, there are no breakouts presented at this depth. So, in this case, a depth of 5547.5 ft of Well 2 is taken as an example to analyze the breakouts and tensile failure problems with the FEM program. B limestone formation is considered as isotropic as introduced in Chapter 3. The FEM program is based on the concept of generalized plane strain and it has the capabilities to study the anisotropic effects from rock mattress with different rock material principal directions, wellbore drilling directions and in-situ stress directions. In this case, east is set as the positive direction of x-axis, north as positive y-direction and up as positive z-direction. The axis of the wellbore is parallel to the z-axis and the wellbore cross section is parallel to the x-y plane. The vertical in-situ stress is in the z-axis direction and the maximum horizontal in-situ stress and minimum horizontal in-situ stress are about 15° anticlockwise to the x-axis and y-axis of the well coordinate system as shown in the Figure 4-1. The inputs of reservoir condition and initial conditions are from the 3D MEM, which are summarized in Table 4-1 and Table 4-2. The wellbore pressure is calculated based on the depth and the mud density. The mud density of Well 2 is 9.2ppg from the field report provided by the operator, which is 0.4784psi/ft.

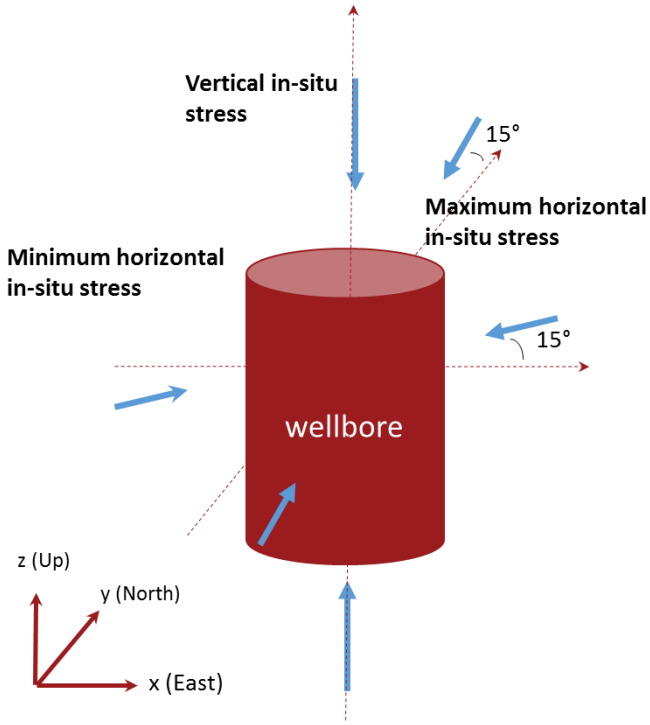

Figure 4-1 Wellbore and in-situ stress states

Table 4-1 Inputs of reservoir condition from the 3D MEM

Formation	Depth, ft	E, Gpa	G, Gpa	v	α	M, psi
B LS	5547.5	52.75	20.81	0.267	0.900	2.36E+06

Table 4-2 Inputs of stress initiation from the 3D MEM

Formation	Depth, ft	σ_z, psi	σ_y, psi	σ_x, psi	P_p, psi	P_w, psi
B LS	5547.5	5653	3537	3643	2581	2654

4.1.2 Results and Analysis

The effective stress, total stress in different directions (tangential, radial and z-direction) near the wellbore and the tangential Terzaghi's effective stress around wellbore are plotted and analyzed. As pore pressure exists, effective stress instead of total stress is used to determine whether the rock fails or not. Terzaghi's effective stress, which is a situation of the effective stress with the Biot's coefficient as 1, maximizes the

reaction of the pore pressure on rock stresses. So, the Terzaghi's effective stress is used to justify the failure status of a rock. Thus, tangential Terzaghi's effective stress is used to determine the shear failure and tensile failure around the wellbore with the Eqs. 2-2 and 2-3 in order to identify if breakouts and drilling-induced fractures happen. Figs. 4-2 and 4-3 present the results of the effective stress and the total stress in tangential, radial and z-directions of wellbore cross section of Well 2 at depth of 5547.5 ft in B limestone formation. Due to the anisotropic in-situ stress, the tangential and radial effective stresses around the wellbore are in elliptical rather than round shape. High tangential effective stress and low radial effective stress are concentrated around the wellbore. Since all the tangential effective stresses are positive, only shear failure might happen at this depth. Hence, breakouts might occur while drilling-induced fracture does not. The maximum and minimum effective stress in z direction locates at N15W and N75E of the wellbore, which are the same with the directions of maximum and minimum horizontal in-situ stress.

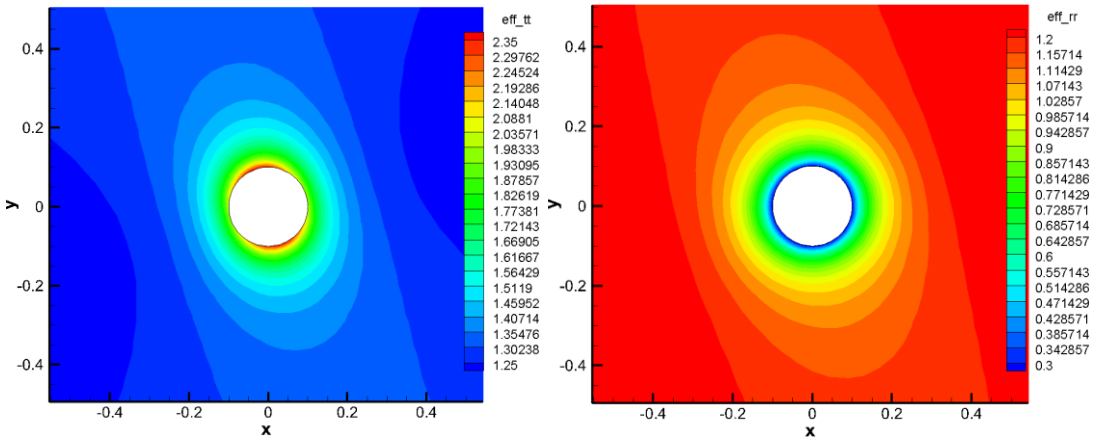

(a) Tangential Stress, 10^3psi (b) Radial Stress, 10^3psi

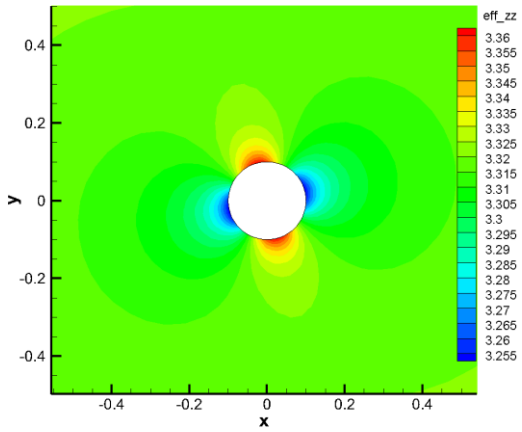

(c) Z-Direction Stress, 10^3psi

Figure 4-2 Effective stress distributions.

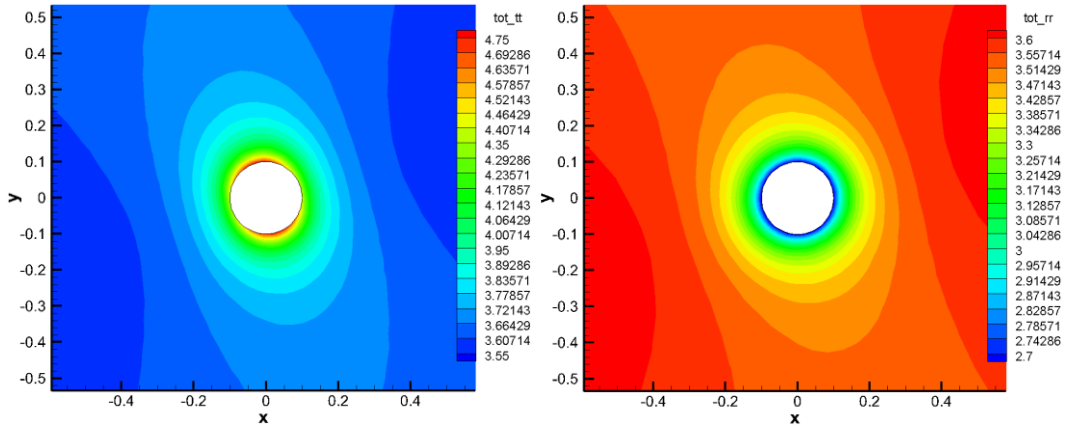

(a) Tangential Stress, 10^3psi

(b) Radial Stress, 10^3psi

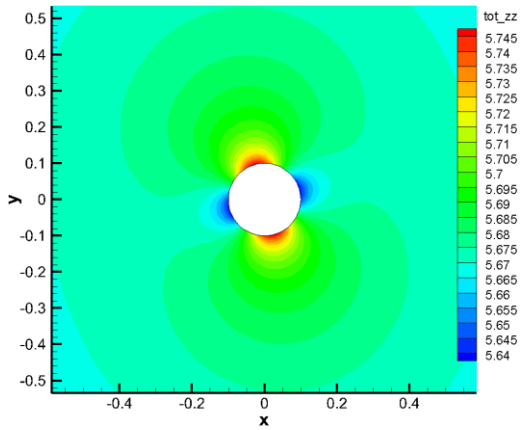

(c) Z-Direction Stress, 10^3psi

Figure 4-3 Total stress distributions.

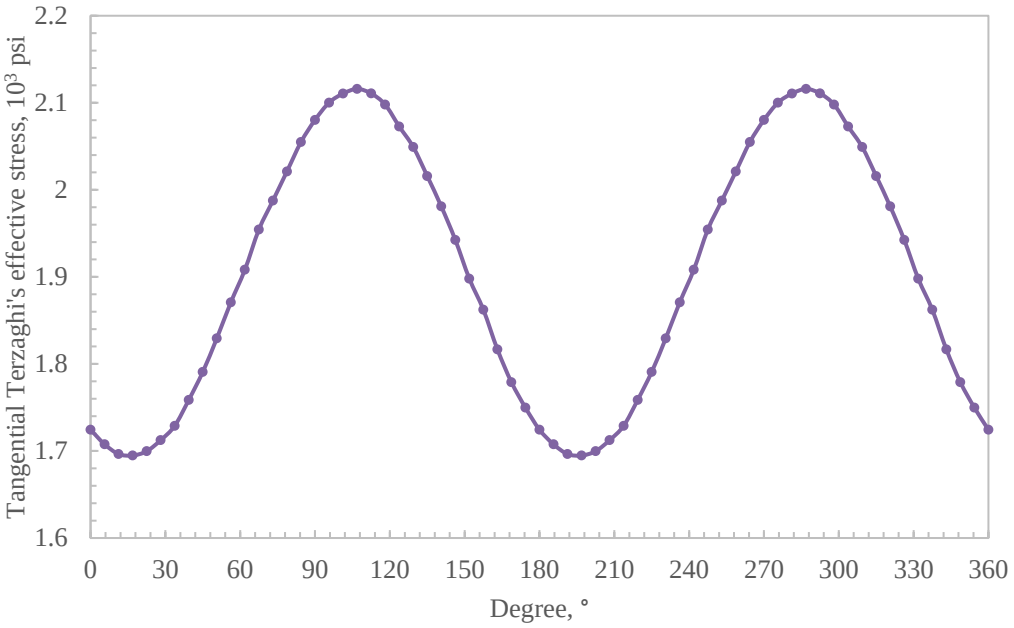

Figure 4-4 Tangential Terzaghi's effective stress distribution around the wellbore.

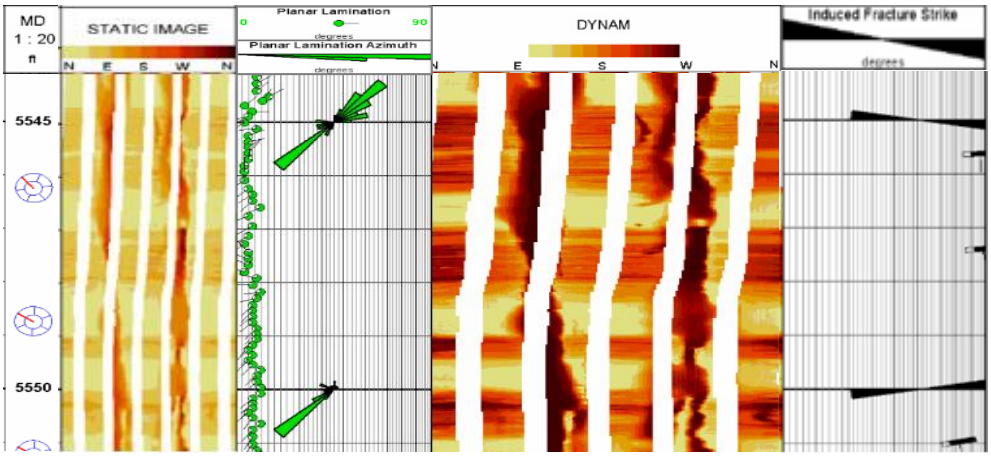

Figure 4-5 Borehole image log of B limestone (at depth of 5547. 5 ft)

Fig 4-4 plots the tangential Terzaghi's effective stress around the wellbore. For this case, the tangential Terzaghi's effective stress is in the range of 1690-2120 psi. The maximum and minimum tangential stresses are at N15W and N75E. Since the minimum

tangential Terzaghi's effective stress is positive (meaning compression), tensile cracking will not occur.

In the borehole image log, the darker color presents higher conductivity, which might be due to faults, fractures and shale beddings. The lighter color presents higher resistivity, which might be the rocks. In the Fig. 4-5, the thin dark lines along the wellbore indicate the drilling-induced fractures which are mainly at east-west direction. The horizontal brown color which is perpendicular to the wellbore is the shale beddings in the reservoir. There are no breakouts presented in this well portion. The orientation of the minimum tangential Terzaghi's effective stresses is close to measurements from the borehole image log. However, the calculated FEM results are different from the failure condition observed from the borehole image log, indicating the horizontal in-situ stresses from the MEM are too close to each other. So, the maximum horizontal in-situ stress from the MEM is underestimated and needs to be calibrated. The calibration approach is to adjust their values in the FEM program to match the borehole image log. The calibrated maximum horizontal in-situ stress is 5500 psi, under which condition the drilling-induced fractures show up and the fracture shape is in good agreement with that from the borehole image log. As shown in Fig. 4-6, the recalculated tangential effective stress has negative values at about east-west direction, indicating tensile failure tendency. In another word, drilling-induced fractures occur at east-west direction with the calibrated in-situ stress. The maximum tangential effective stress is at about north-south direction. UCS is used to identify shear failure at the positions of maximum tangential effective stress. The recalculated stress status with the calibrated in-situ stress are presented in Figs. 4-6 and 4-7.

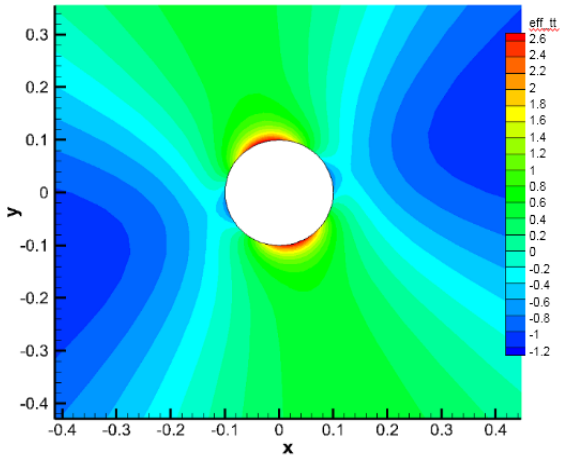

(a) Tangential Stress, 10^3psi

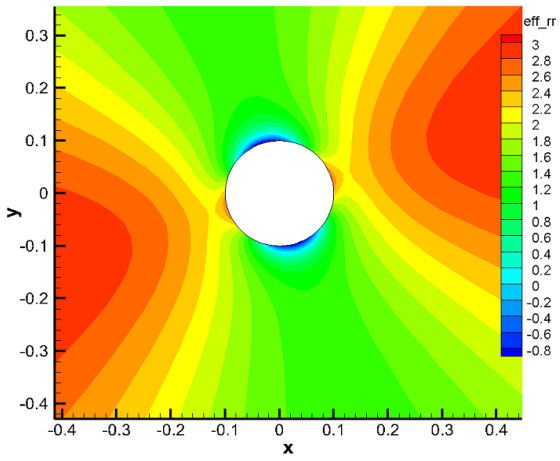

(b) Radial Stress, 10^3psi

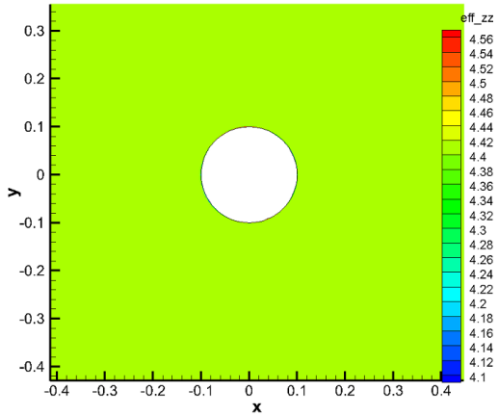

(c) Z-Direction Stress, 10^3psi

Figure 4-6 Recalculated effective stress distributions after calibration.

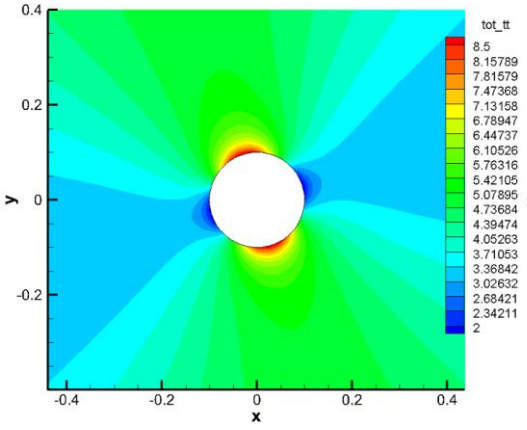

(a) Tangential Stress, 10^3psi

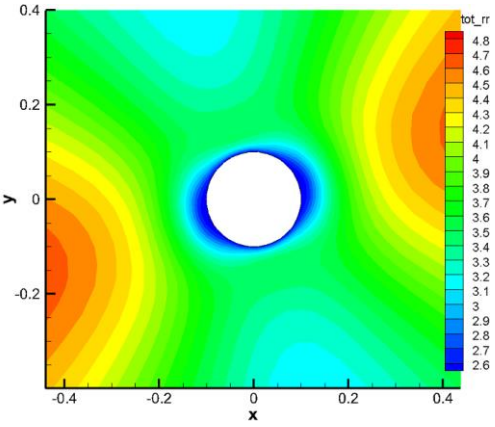

(b) Radial Stress, 10^3psi

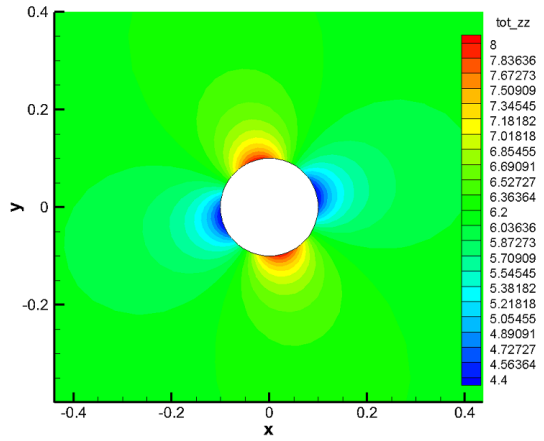

(c) Z-Direction Stress, 10^3psi

Figure 4-7 Recalculated Total stress distributions after calibration.

4.1.3 Summary

From previous analysis, due to the assumptions made in the calculation process, the inconsistency between the calculated FEM results and borehole image log indicates the original obtained in-situ stresses from the MEM needs to be calibrated. The calibrated in-situ stress and pore pressure at the depth of 5547.5 ft are summarized in Table 4-3. The vertical in-situ stress is estimated from overburden. The magnitude of minimum horizontal in-situ stress is calculated basing on the elasticity theory and calibrated by the HF data. And the maximum horizontal in-situ stress magnitude is calibrated with the FEM program and borehole image log measurements. The directions of minimum and maximum horizontal in-situ stress are obtained from the HF analysis and microseismic measurements. The obtained directions of in-situ stress are in a good agreement with the borehole image log measurements. Therefore, the calibrated in-situ stresses can be used as inputs for further applications.

Table 4-3 Calibrated stress states in the 3D MEM

Formation	Depth, ft	σ_z, psi	σ_y, psi	σ_x, psi	P_p, psi

B LS	5547.5	5653	3537	5500	2581

4.2 Hydraulic Fracturing (HF) Modeling

In this case, a hydraulic fracturing treatment is modeled with StimPlan software. The calibrated 3D MEM provides the input of rock mechanical properties and stress conditions, and the other reservoir physical properties are obtained from field reports. The HF is reproduced by simulation to fit the microseismic measurement. Then the trend of fracture shapes with various injection rates and volumes is studied.

4.2.1 Problem statement

The horizontal section of Well 12 is located in B limestone formation, of which thickness is about 300 ft. In the stimulation operations, the hydraulic fractures have grown into the confining zones according to the evaluation of microseismic measurement (shown in Fig. 4-13). The objective of this simulation study is to analyze the HF process and investigate the effects of the injection rate and volume on hydraulic fracture shapes.

A 3D MESM around the horizontal well of Well 12 area is cut from the 3D MEM and is applied to model the hydraulic fracturing process. This MESM carries all the properties calculated from the original MEM as shown in Fig. 4-8. The rock and reservoir properties obtained from the sector model are incorporated into the StimPlan software to simulate the HF process. The inputs from the MESM is shown in the Table 4-4 and 4-5. The constructed MEM well reveals the reservoir heterogeneity so that the generated heterogeneous model can be incorporated into other software for further study. However, the heterogeneity of the formation cannot be considered in some software due to their limitation. In this work, the reservoir rock formation studied in the

StimPlan software for HF modeling is assumed as uniform, homogeneous and isotropic. The dominated values of the properties from the MEM are applied as inputs for the HF simulation. The discrete natural fracture network is not considered in this simulation either, due to the dramatically increased computational intensity and numerical instability of the Stimplan software.

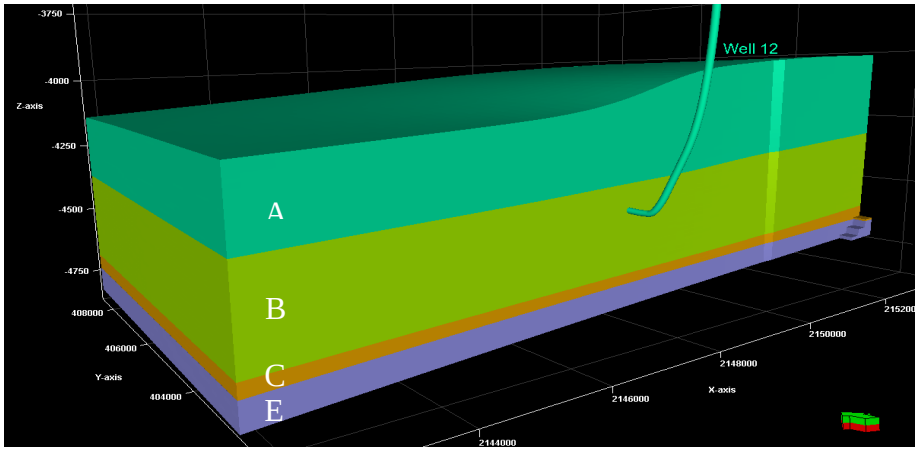

Figure 4-8 The 3D MESM around the Well 12

Table 4-4 Inputs from the MESM

Layer	TVD Depth to Top of Zone, ft	Type	Stress at Top of Zone, psi	Young's Modulus, MMpsi	Poisson's Ratio	Fluid Loss Coefficient, ft/root(min)
1	5246	Silty	5528	3.978	0.27	0.0093
2	5491	Oil	6003	7.910	0.26	0
3	5792	Shale	6167	2.320	0.16	0.0080

Table 4-5 Reservoir Properties from the field report

Casing ID, in	4.0
Initial reservoir pressure, psi	2408
Current reservoir pressure, psi	2165
Bottomhole injection temperature, °F	137
Porosity, %	10

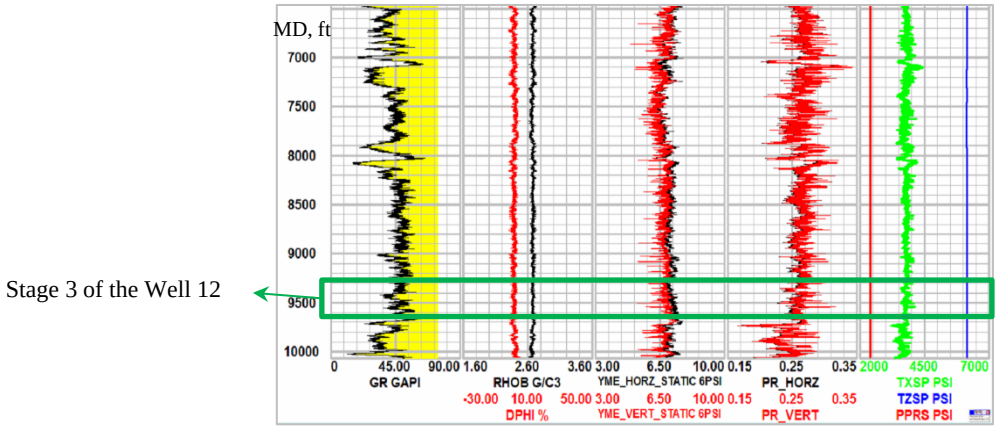

Figure 4-9 Logs of inputs around the Well 12 from the 3D MESM

In this study, the hydraulic fracture operation of Stage 3 of Well 12 is modeled to verify the simulation inputs and process. Stage 3 is marked in the green box in the Fig. 4-9. The total length of stage 3 is 300 ft. The Stage 3 has four clusters of perforations, with 84-ft-length spacing and 43-ft-distance away from the ends of this stage. The HF fluid parameters and pump schedule are obtained from the field HF design and operation report. The fluid is mainly composed of 12.5% HCl acid and slick water. The proppant is white sand 30/50, whose grain size is 300-600μm. The field pump schedule for Stage 3 of the Well 12 is shown in Table 4-6, from which it can be found that the main injection rate for Stage 3 of the Well 12 of field HF operation is 75bpm.

Table 4-6 Field pump schedule for Stage 3

Stage	Fluid Type	Fluid Volume (gal)	Proppant Conc. (ppa)	Slurry rate (bpm)	Stage pump time (min)
1	Slick water	10000		20	11.91
2	12.5% HCI Acid	1500		10	3.57

3	Slick water	35000		75	11.11
4	Slick water	128000	0.3	75	40.64
5	Slick water	10000	0.5	75	3.17
6	Slick water	5000		75	1.59
7	Slick water	5000		75	1.59
8	Slick water	35000		75	11.11
9	Slick water	128000	0.3	75	40.64
10	Slick water	10000	0.5	75	3.17
11	Slick water	5000		75	1.59
12	Slick water	5000		75	1.59
13	Slick water	35000		75	11.11
14	Slick water	128000	0.3	75	40.64
15	Slick water	10000	0.5	75	3.17
16	Slick water	11920		75	3.78
Total		562420			190.38

4.2.2 Hydraulic fracturing modeling

In this section, the growth of a hydraulic fracture is simulated, i.e., one cluster of perforations of Stage 3. The injection fluid volume and rate is assumed evenly allocated to each perforation in Stage 3. From the information of this area, the confining zones above and below the pay zone B might connect with some aquifer or contain natural fractures, since significant water production is observed, leading to fluid leak off in the confining zones during hydraulic fracturing. However, fluid loss coefficient is hard to be measured during the field stimulation so it is generally assumed or used as a matching parameter. In this work, we obtained a fluid loss coefficient as 0.0093 and 0.008 ft/root(min) in the confining zones and that matches the modeled fracture shape with the microseismic measurement.

The simulated fracture shape and its propagation in different time are shown in the Fig. 4-10. The left-hand side images in Fig. 4-10 present the target formation (B limestone) marked in green, the confining silty zone is marked in yellow and confining shale zone in grey. The horizontal axis is the reservoir pressure and the vertical axis

represents the true vertical depth. On the right hand of the figures, one wing of the hydraulic fracture is plotted (symmetric growth is assumed). Same with field operation, the total injection duration time is 188 minutes. The shapes of hydraulic fractures at four time steps of 10 mins, 1 hour, 1.5 hours and 3 hours are presented. Fig. 4-11 plots the height and length of the simulated hydraulic fracture as a function of injection time. The injection rate is the actual field operation rate. From Fig. 4-10 and 4-11, it can be observed that the hydraulic fracture opens at about 20 min. In the first 30 mins, the fracture grows primarily in radial direction. The growth rate in vertical direction is larger than in horizontal direction. After the fracture height grows beyond the thickness of the target zone at 30 min, the growth speed of fracture height starts to slow down. At 70 min, the fracture reaches its maximum height of 426 ft and then only the fracture length growth. The half-length of the hydraulic fracture reaches 694 ft at the end of the injection operation. The maximum fracture width is about 0.289 in and locates at near wellbore region. The fracture width reduces drastically near the wellbore and then gradually to fracture tip.

The modeled fracture length well matches the right-hand side of the hydraulic fracture length from the microseismic result (Fig. 4-12), which is about 670 ft. But in the microseismic measurement result, the hydraulic fracture is not symmetric to the wellbore where the left-hand side of the hydraulic fracture half-length is much shorter than the right-hand side. This might be due to the micro-earthquake data gathering is limited by the tools so the hydraulic fracture shape is not fully represented by the microseismic data. The height of the simulated hydraulic fracture matches well with the microseismic measurement which is about 420 ft, as shown in Fig. 4-13.

According to the report, the maximum treating pressure is around 7,900 psi. The maximum bottom hole injection pressure from the simulation result is 7750 psi, as shown in Fig. 4-14, which is in good agreement with the field operation data, indicating reasonable input in the hydraulic fracturing simulation work.

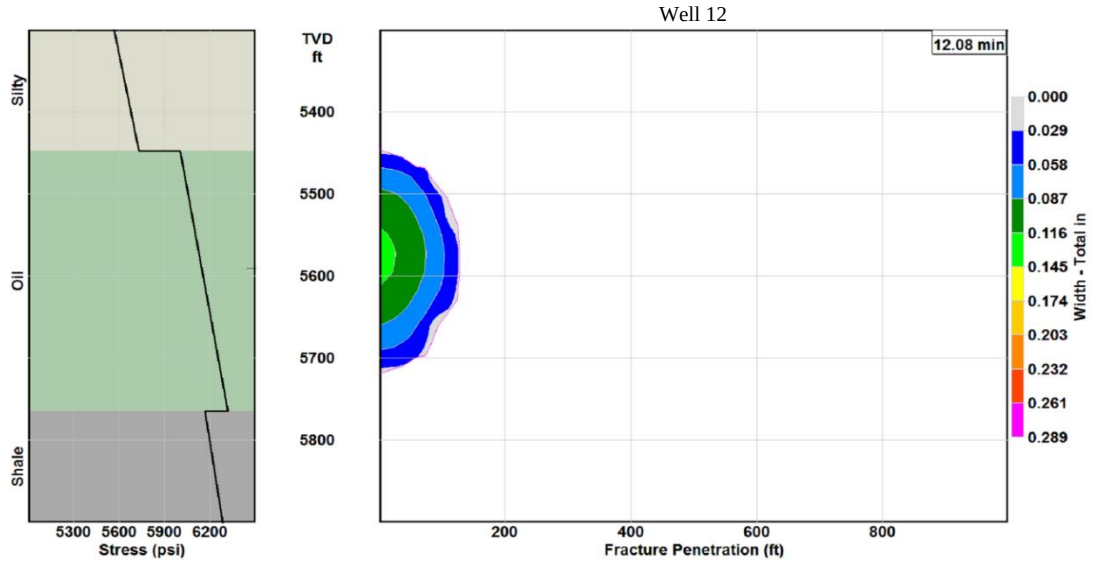

(a) Hydraulic fracture shape at t=12.08 min

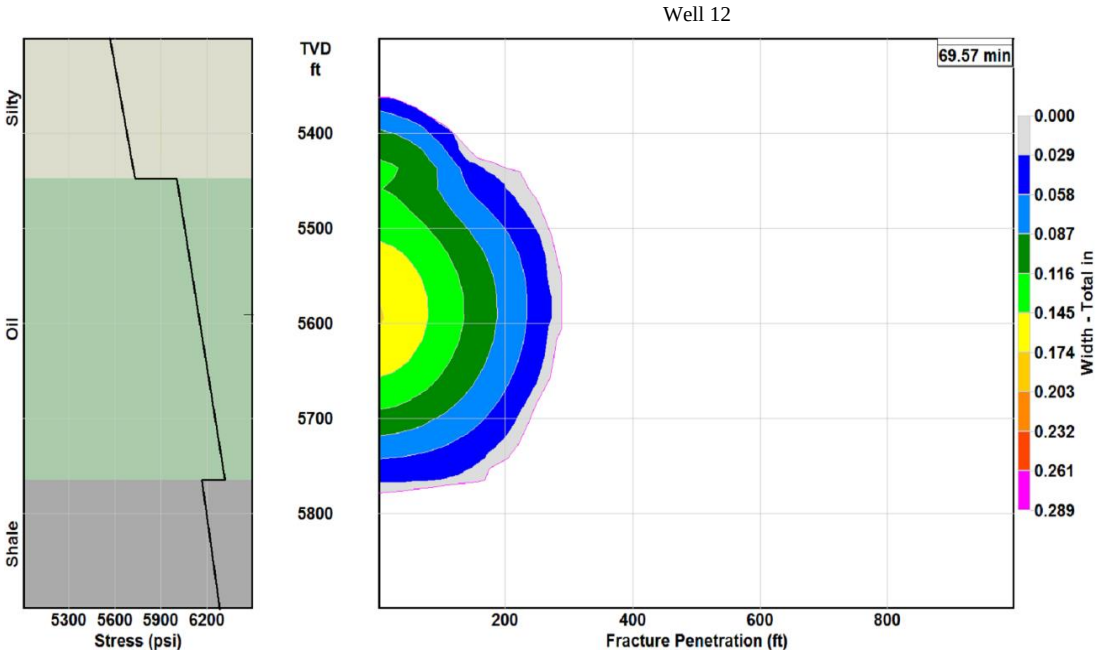

(b) Hydraulic fracture shape at t=69.57 min

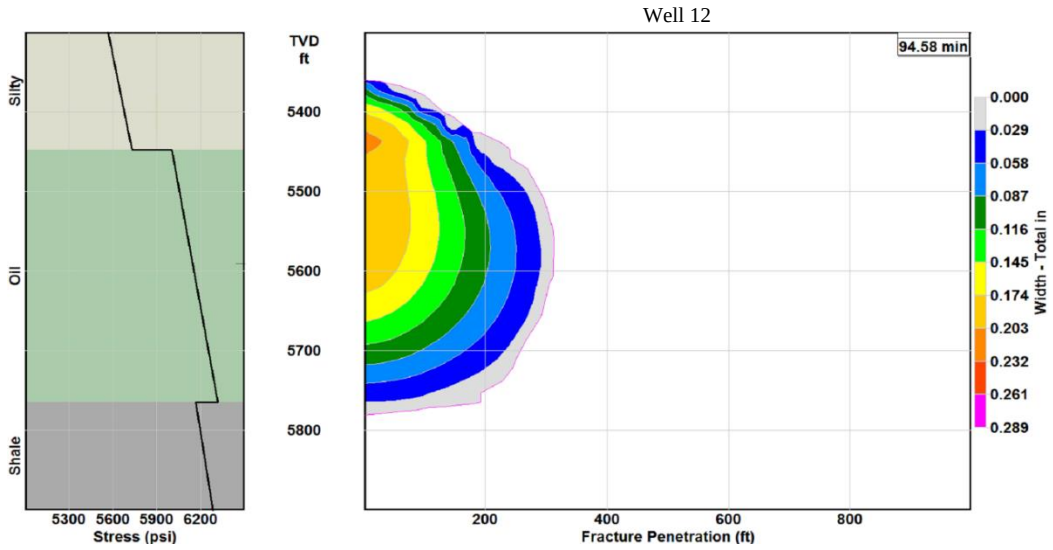

(c) Hydraulic fracture shape at t=94.58 min

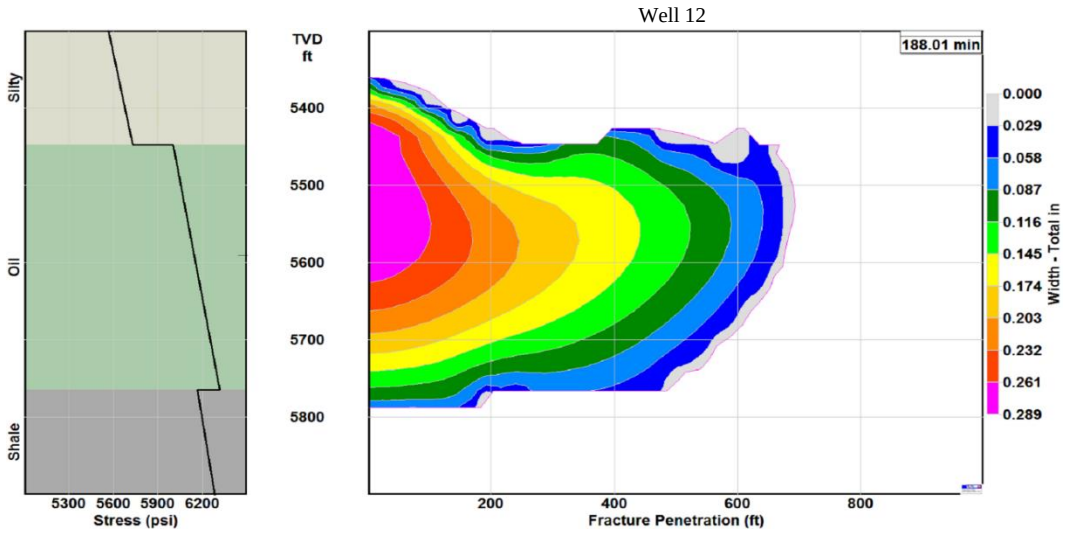

(d) Hydraulic fracture shape at t=188.01min

Figure 4-10 Cross section view of hydraulic fracture half-length Vs width at different time.

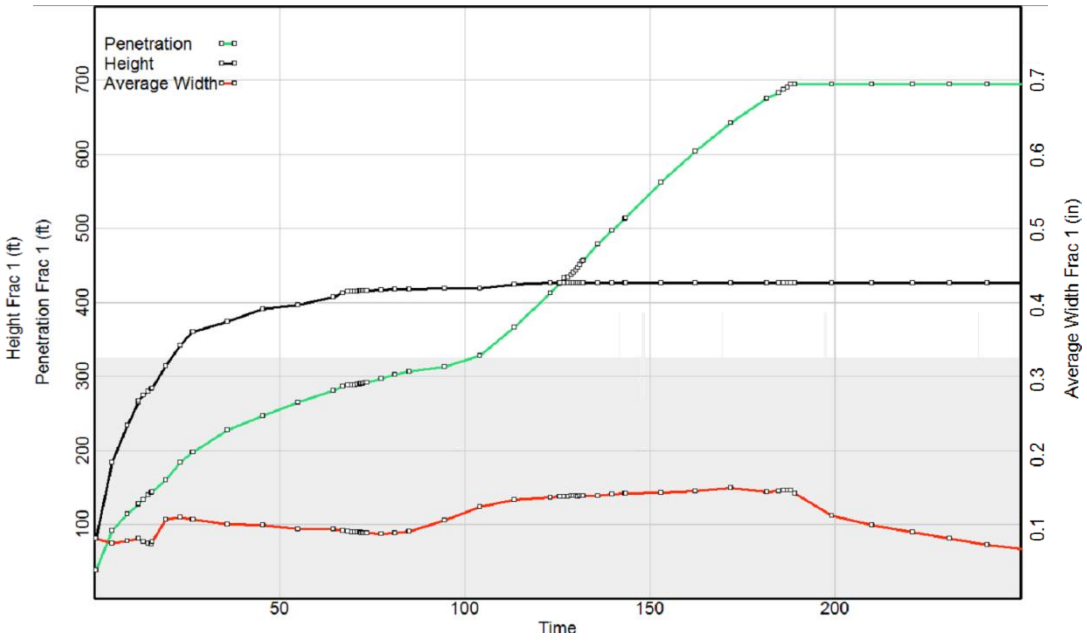

Figure 4-11 Fracture height, length and average width with time

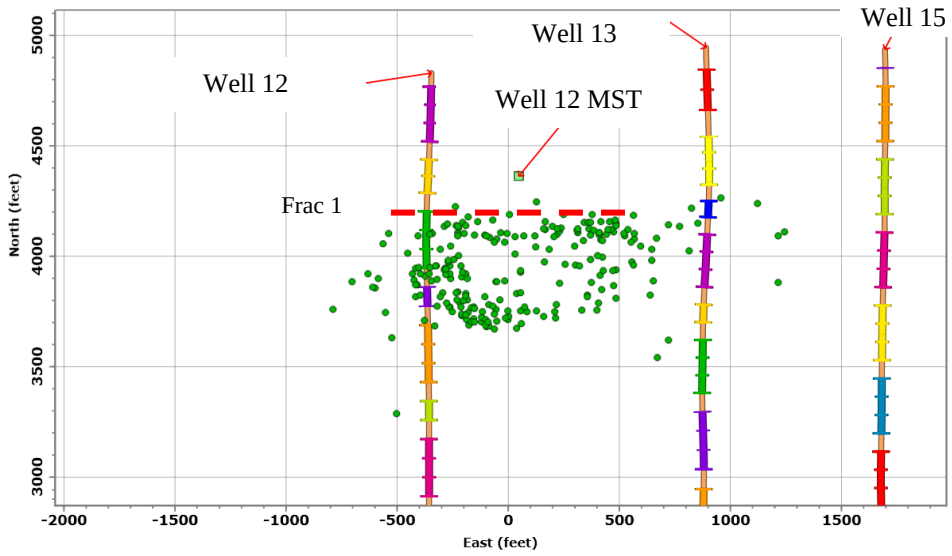

Figure 4-12 Bird view of hydraulic fracture shape of Stage 3 Well 12 from microseismic measurement

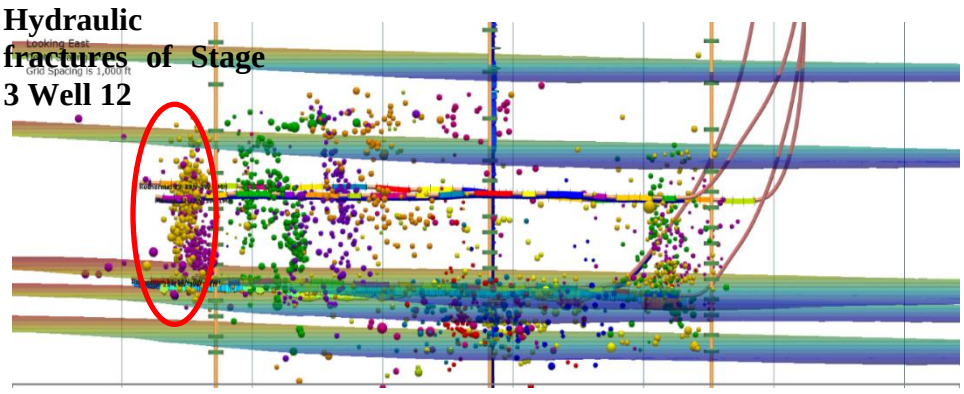

Figure 4-13 Side view of hydraulic fracture shape of Stage 3 Well 12 from microseismic measurement

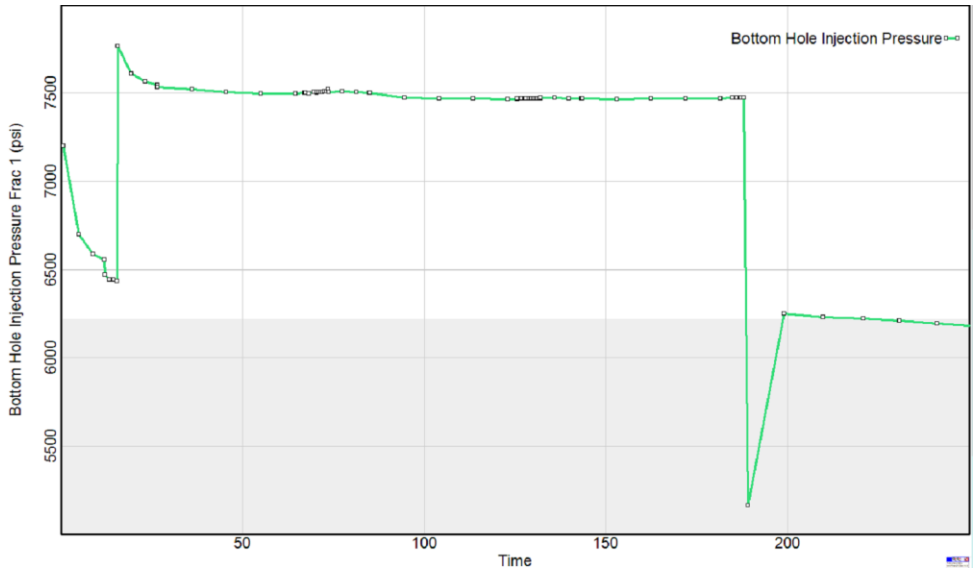

Figure 4-14 Bottom hole injection pressure of Stage 3 Well 12.

The next step in this section is to investigate the impacts of injection rate and volume to the fracture height and length. First, the same total injected fluid volume is assumed, and 80% and 60% of the fluid injection rates are applied. Then with the same injection rate, the hydraulic fracture height and length are studied with 80% and 60% of the total injection volume.

Figs. 4-15 through 4-17 show the hydraulic fracture shapes for different injection rates. Table 4-7 summarizes the fracture shapes, from which it can be observed that with the same total injected fluid volume the lower of the injection rate the shorter of fracture height and the longer of the fracture length.

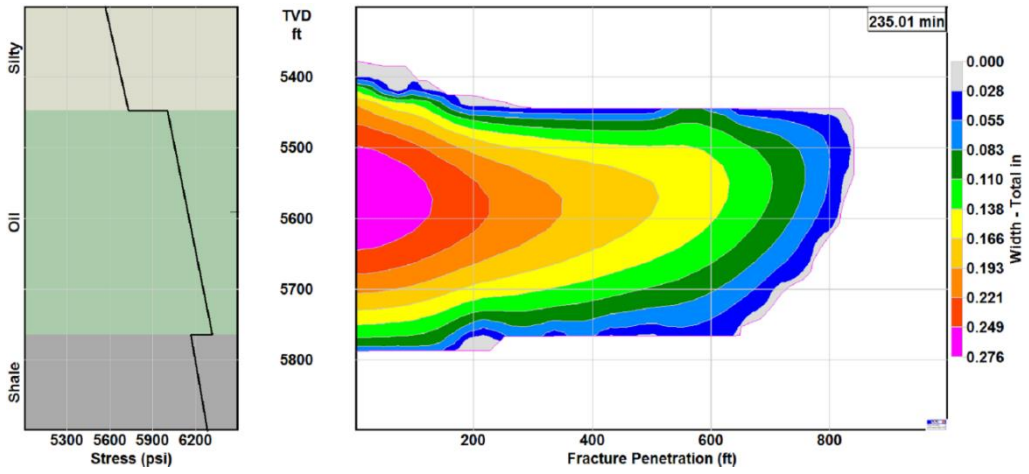

Figure 4-15 Hydraulic fracture shape with 80% of the field injection rate

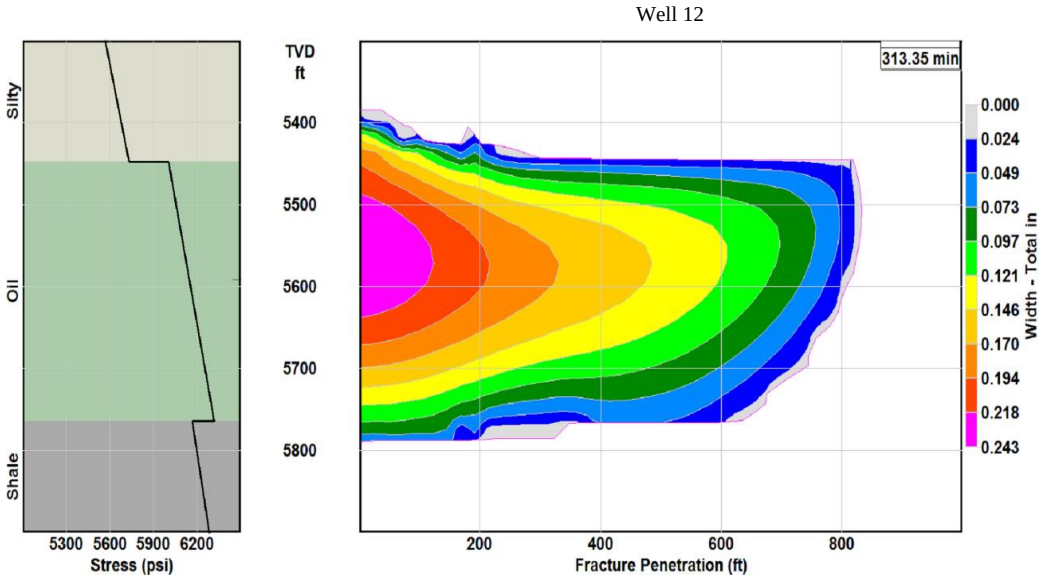

Figure 4-16 Hydraulic fracture shape with 60% of the field injection rate

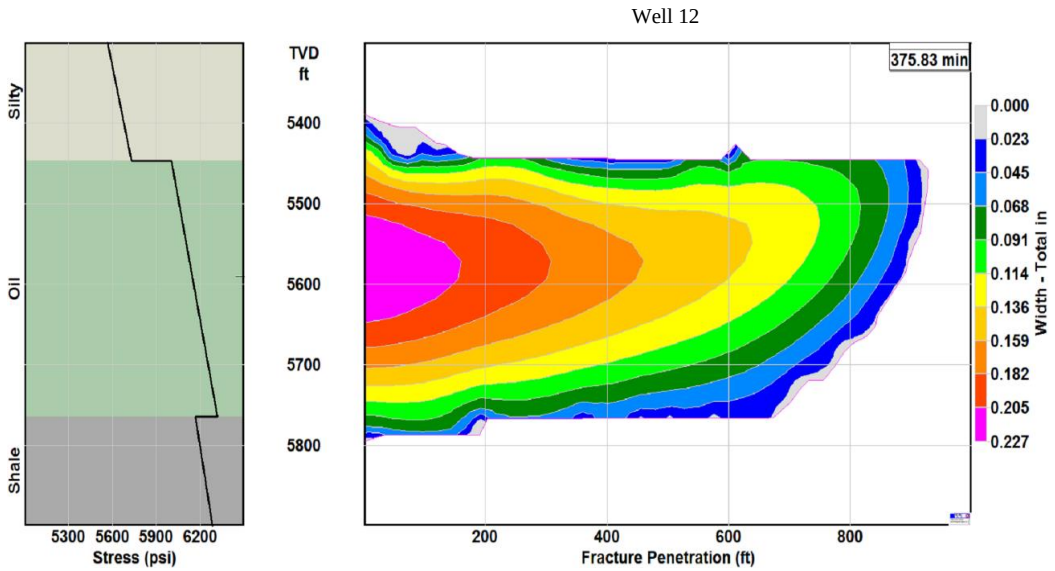

Figure 4-17 Cross section view of hydraulic fracture shape with 50% of the field injection rate

Table 4-7 Hydraulic fracture shape with different injection rate

	Microseismic measurement	Field injection rate (simulated)	80% of the Field injection rate	60% of the Field injection rate	50% of the Field injection rate
Half length, ft	670	694.2	841.7	843	929
Max fracture height, ft	420	426	408.3	404.1	398.7
Average width at end of pumping, in	-	0.15	0.14	0.12	0.13
Average conductivity, md-ft	-	13.8	20.7	20.6	20.9
Efficiency at end of pumping schedule	-	0.29	0.34	0.3	0.32

Similarly, the effects of total injection volume on the fracture shapes are also studied. Table 4-8 summarizes the results. From the hydraulic fracture shapes, with the same injection rate, reducing the total injection volume leads to shorter fracture height and fracture length.

Table 4-8 Hydraulic fracture shape with different total injection volume

	Field total injection volume (simulated)	80% of the Field total injection volume	60% of the Field total injection volume
Half length, ft	694.2	636.7	548
Max fracture height, ft	426	418.6	407.8
Average width at end of pumping, in	0.15	0.15	0.13
Average conductivity, md-ft	13.8	12.5	18.1
Efficiency at end of pumping schedule	0.29	0.34	0.35

By comparing the values in Tables 4-7 and 4-8 that, both reducing the injection rate and total volume can shorten the fracture height, but reducing the injection rate is more effective in hindering the fracture growth into the confining zones. The fracture length increases with the decrease of injection rate but it decreases with the decrease of injection volume. The trend is clearer as the curves plotted in Fig. 4-18, which shows the maximum fracture height and length at various injection volumes and rates. An injection rate of 60 bmp (80% of the field operation rate) decreases the injection volume from 100% to 80% without much effect on reducing the fracture height, but reduces the fracture length from 842 ft to 713 ft. Therefore, by evaluating the results shown in Fig. 4-18, an injection rate of 60 bpm with the original injection volume would be recommended for the hydraulic fracturing treatment. Fig. 4-18 can also be an instruction for selecting appropriate injection rate and volume for a horizontal well in the same formation but with different reservoir pay thickness.

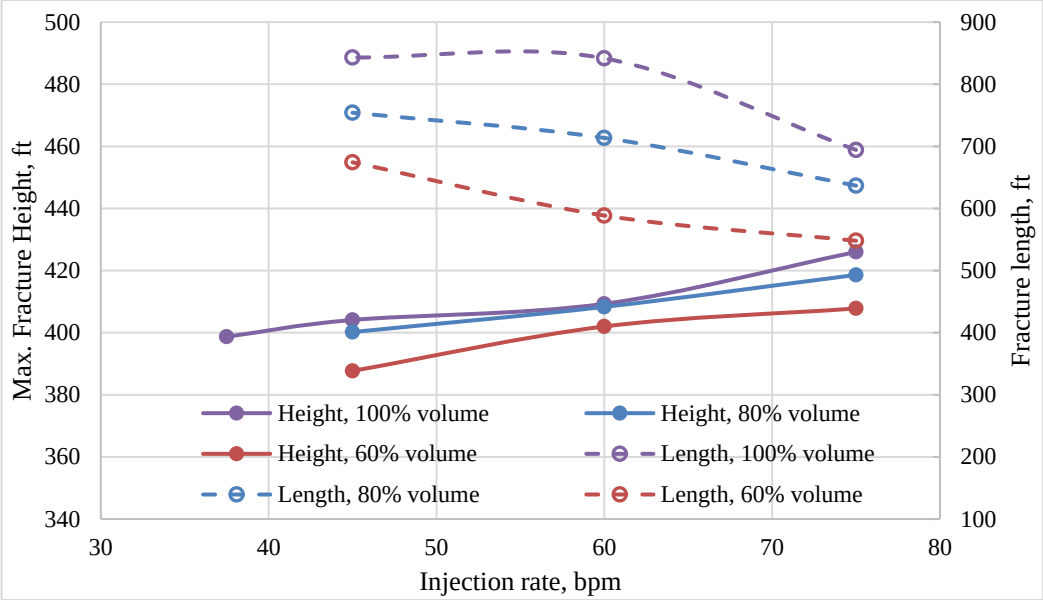

Figure 4-18 Maximum fracture height and fracture length at various injection rate and volume

Recalling the pay zone thickness of the target limestone is 300 ft, it can be found from Tables 4-7 and 4-8 that even when the injection rate is reduced to 50% (or the total injection volume is reduced to 60%), the modeled fracture height is still larger than 300 ft. There are several reasons for these modeling results: firstly, in StimPlan the closure pressure and stress difference in different zones dominates the fracture shape and analysis. In this study, the minimum horizontal stress is calculated from the overburden pressure according to the theory of elasticity without considering tectonic, so the stress differences of minimum horizontal stress in different zones are derived from the overburden pressure without taking account into tectonic; secondly, from Table 4-4 it can be found the Young's modulus of confining zones (layers 1 and 3) are much smaller than that of the target zone (layer 2), so the calculated strengths of confining zone are also much smaller than the target zone, according to Eq. 3-19, indicating the confining zones are easier to be fractured; thirdly, from the MEM there are many natural fractures

in the target formation which are not considered in the hydraulic fracturing simulations due to the numerical instability of the model and the computational costs, which may lead to overestimated Young's modulus of the target limestone formation.

Hence, from this hydraulic fracturing simulation, without a stress barrier it is difficult to control the hydraulic fracture in the target formation without penetrating the confining zones. But a lower injection rate would help.

Conclusion and summary

The following conclusions can be drawn from this thesis:

1. The Mechanical Earth Model (MEM) is a powerful tool integrating reservoir geological description, petrophysical characterization as well as the in-situ geomechanical situation that can be used for optimizing drilling design as well as hydraulic fracturing treatment. Commercial software such as Petrel and Jewel Suite or any 3D FEM can be used to construct the MEM.
2. A workflow to develop a 3D MEM using the Petrel software has been developed. First, a series of 1D mechanical earth models for a number of wells are constructed by calculating the overburden stress and pore pressure, mechanical rock properties, in-situ stress as well as failure mechanisms from well logs and core characterizations. A 3D mechanical earth model is then built by correlating the 1D MEM and incorporating the geological conditions through stratigraphy modeling, structural framework construction, property modeling as well as fracture modeling.
3. A 3D Mechanical Earth Model (MEM) for a portion of a basin in Central Oklahoma has been developed. 1D MEMs that describe the rock properties, pore pressure and stress status for 9 wells in the basin were firstly constructed using available well logs and core description. And a 3D MEM was then generated by following the workflow. The B limestone is primarily modeled.
4. A 3D sector model has been cut out from the 3D MEM to perform wellbore stability and hydraulic fracturing case studies. The stress state around the wellbore of the vertical Well 2 is modeled with a FEM program using the

reservoir condition inputs from the 3D MEM. The Terzaghi's effective stresses around the wellbore are computed and analyzed to identify breakouts and tensile cracks and their positions. There are drilling-induced fractures in the studied well depth according to the analysis. The in-situ stresses calculated from the 3D MEM are calibrated by comparing the borehole image log. And the calibrated in-situ stresses are then used as inputs to recalculate the stress status with the FEM program. The calibrated maximum horizontal in-situ stress is 5500 psi, which was 3643 before calibration.

5. By incorporating the 3D sector mechanical earth model with the hydraulic fracturing simulation, a hydraulic fracture of stage 3 of Well 12 has been simulated. All the simulation results match well the microseismic measurements. Field results and numerical simulations indicate the hydraulic fractures penetrate the confining shales due to the high injection rate (the height of the hydraulic fracture is larger than the thickness of the Mississippi limestone). The impacts of injection rate and volume on fracture shapes are studied. The results of both reducing the injection rate and total volume can shorten the fracture height, but reducing the injection rate is more effective in hindering the fracture grows to the confining zones. For the fracture length, it increases with the decrease of injection rate but decreases with the injection volume.

References

Afsari, M., Amani, M., Razmgir, S. A. M., Karimi, H., & Yousefi, S. (2010, January). Using drilling and logging data for developing 1d mechanical earth model for a mature oil field to predict and mitigate wellbore stability challenges. In International Oil and Gas Conference and Exhibition in China. Society of Petroleum Engineers.

Afsari, M., Ghafoori, M., Roostaeian, M., Haghshenas, A., Ataei, A., & Masoudi, R. (2009, January). Mechanical Earth Model (MEM): an effective tool for borehole stability analysis and managed pressure drilling (Case Study). In SPE Middle East Oil and Gas Show and Conference. Society of Petroleum Engineers.

Athy, L. F. (1930). Density, porosity, and compaction of sedimentary rocks. AAPG Bulletin, 14(1), 1-24.

Bradford, I. D. R., Fuller, J., Thompson, P. J., & Walsgrove, T. R. (1998, January). Benefits of assessing the solids production risk in a North Sea reservoir using elastoplastic modeling. In SPE/ISRM Rock Mechanics in Petroleum Engineering. Society of Petroleum Engineers.

Brady, B. H., & Brown, E. T. (2013). Rock mechanics: for underground mining. Springer Science & Business Media.

Chang, C., Zoback, M. D., & Khaksar, A. (2006). Empirical relations between rock strength and physical properties in sedimentary rocks. Journal of Petroleum Science and Engineering, 51(3), 223-237.

Dolton, G. L., & Finn, T. F. (1989). Petroleum geology of the Nemaha Uplift, central mid-continent (No. 88-450-D). Dept. of the Interior, US Geological Survey.

Doyen, P. M., Malinverno, A., Prioul, R., Hooyman, P., Noeth, S., den Boer, L., ... & Wervelman, R. (2003, January). Seismic pore pressure prediction with uncertainty using a probabilistic mechanical earth model. In 2003 SEG Annual Meeting. Society of Exploration Geophysicists.

Eaton, B. A. (1975, January). The equation for geopressure prediction from well logs. In Fall Meeting of the Society of Petroleum Engineers of AIME. Society of Petroleum Engineers.

Fattahpour, V., Pirayehgar, A., Dusseault, M. B., & Mehrgini, B. (2012, January). Building a Mechanical Earth Model: a Reservoir In Southwest Iran. In 46th US Rock Mechanics/Geomechanics Symposium. American Rock Mechanics Association.

Hudson, J. A., & Harrison, J. P. (1997). Engineering Rock Mechanics: An Introduction to the Principles. Elsevier Science Ltd.

Kirsch. (1898). The Theory of Elasticity and the Need of the Strength of Materials(Trans.). Journal of the Association of German Engineers 42: 797-807.

Jaeger, J. C., Cook, N. G., & Zimmerman, R. (2009). Fundamentals of rock mechanics. John Wiley & Sons.

Janis, M., Liu, J., & Ghassemi, A. (2016). Reservoir geomechanics model for EGS. In Geothermal Resource Council 2016 Annual Meeting. U.S. Department of Energy.

Lang, J., Li, S., & Zhang, J. (2011, January). Wellbore stability modeling and real-time surveillance for deepwater drilling to weak bedding planes and depleted reservoirs. In SPE/IADC Drilling Conference and Exhibition. Society of Petroleum Engineers.

Lee, D. W., Singh, V., & Berard, T. (2009, January). Construction of a Mechanical Earth Model and Wellbore Stability Analysis for a CO2 Injection Well. In SPE International Conference on CO2 Capture, Storage, and Utilization. Society of Petroleum Engineers.

Lee, D., Cassanelli, J. P., Frydman, M., Palacio, J., Delgado, R., & Collins, B. (2003, January). Using a Dynamic Mechanical Earth Model and Integrated Drilling Team to Reduce Well Costs and Drilling Risks in San Martin Field. In SPE Annual Technical Conference and Exhibition. Society of Petroleum Engineers.

Liang, B., Khan, S., Puspita, S. D., Tran, T., Du, S., Blair, E., & Rives, S. (2016, September). Improving Unconventional Reservoir Factory-Model Development by an Integrated Workflow with Earth Model, Hydraulic Fracturing, Reservoir Simulation and Uncertainty Analysis. In Unconventional Resources Technology Conference. Unconventional Resources Technology Conference.

Lu, C. (2013). Effect of Rock Transverse Isotropy on Stress Distribution and Wellbore Fracture. Master thesis, Texas A&M University.

Moos, D., & Barton, C. A. (1990). In-Situ Stress and Natural Fracturing at the INEL Site. Idaho: US Department of Energy Report EGG-NPR-10631.

Moos, D., & Zoback, M. D. (1990). Application to Continental, Deep Sea Drilling Project, and. Journal of Geophysical Research, 95(B6), 9305-9325.

Norris, A. N., & Sinha, B. K. (1993). Weak elastic anisotropy and the tube wave. Geophysics, 58(8), 1091-1098.

Perchikolaee, R. S., Shadizadeh, R. S., Shahryar, K., & Kazemzadeh, E. (2010). Building a precise mechanical Earth Model and its application in drilling operation optimization: A case study of Asmari formation in Masuri oil field. In Proceeding of the CPE/SPE International Oil and Gas Conference and Exhibition, June (pp. 8-10).

Plumb, R., Edwards, S., Pidcock, G., Lee, D., & Stacey, B. (2000, January). The mechanical earth model concept and its application to high-risk well construction projects. In IADC/SPE Drilling Conference. Society of Petroleum Engineers.

Samson, P., Casaux, J. M., Cavailles, B., Klein, F., Larribau, E., Lopez, F., & Morandini, F. (1998). Demystifying 3D Earth Modelling. In SEG Technical Program Expanded Abstracts 1998 (pp. 2078-2081). Society of Exploration Geophysicists.

Sayers, C. M. (2008). The elastic properties of carbonates. The Leading Edge, 27(8), 1020-1024.

Sayers, C. M., Russell, C. L., Pelorosso, M., Adachi, J., Pastor, J. A. A., Singh, V., ... & Hooyman, P. J. (2009, January). Determination of rock strength using advanced sonic log interpretation techniques. In SPE Annual Technical Conference and Exhibition. Society of Petroleum Engineers.

Schoenberg, M., Muir, F., & Sayers, C. (1996). Introducing ANNIE: A simple three-parameter anisotropic velocity model for shales. Journal of Seismic Exploration, 5(1), 35-49.

Schön, J. H. (1998). Physical properties of rocks: fundamentals and principles of petrophysics. Pergamon.

Spence, G. H., Couples, G. D., Bevan, T. G., Aguilera, R., Cosgrove, J. W., Daniel, J. M., & Redfern, J. (2014). Advances in the study of naturally fractured hydrocarbon reservoirs: a broad integrated interdisciplinary applied topic. Geological Society, London, Special Publications, 374(1), 1-22.

Wang, Z. (2000). Dynamic versus static elastic properties of reservoir rocks. Seismic and Acoustic Velocities in Reservoir Rocks, SEG Geophysics Reprint Series, No. 19.

Yale, D. P., & Jamieson Jr, W. H. (1994, January). Static and dynamic mechanical properties of carbonates. In 1st North American Rock Mechanics Symposium. American Rock Mechanics Association.

Yasar, E., & Erdogan, Y. (2004). Correlating sound velocity with the density, compressive strength and Young's modulus of carbonate rocks. International Journal of Rock Mechanics and Mining Sciences, 41(5), 871-875.

Zhang, J. (2011). Pore pressure prediction from well logs: Methods, modifications, and new approaches. Earth-Science Reviews, 108(1), 50-63.